Novel delivery system with a dual–trigger release of savory essential oil by mesoporous silica nanospheres and its possible targets in leukemia cancer cells: in vitro study

Khaled AbouAitah[1*], Heba A. Hassan[2], Naglaa M. Ammar[2], Doha H. Abou Baker[1], Imane M. Higazy[3], Olfat G. Shaker[4], Ahmed A. A. Elsayed[1] and Abeer M. E. Hassan[5]

*Correspondence:
ke.abouaitah@nrc.sci.eg

[1] Medicinal and Aromatic Plants Research Department, Pharmaceutical and Drug Industries Research Institute, National Research Centre (NRC), Dokki, Giza 12622, Egypt
[2] Therapeutic Chemistry Department, Pharmaceutical and Drug Industries Research Institute, National Research Centre (NRC), Dokki, Giza 12622, Egypt
[3] Department of Pharmaceutical Technology, Pharmaceutical and Drug Industries Research Institute, National Research Centre (NRC), Dokki, Giza 12622, Egypt
[4] Medical Biochemistry and Molecular Biology Department, Faculty of Medicine, Cairo University, Cairo 11511, Egypt
[5] Chemistry Department, Faculty of Pharmacy, October 6 University, Giza, Egypt

Abstract

Introduction: Essential oils (EOs) are complex structures and possess several pharmacological effects. Nanomedicine offers a solution for their major limitations, including poor solubility, volatility, and non–controlled release, preventing their clinical use.

Methods: Here, we developed a novel delivery system by nanoformulations that were prepared by impregnating savory essential oil (SA) into mesoporous silica nanoparticles (MSNs). The nanoformulations were characterized and examined for their anticancer activities on cancer cells (HepG2 liver and HL60 leukemia cells) and MRC5 normal cells. We further tested the mechanisms of action and possible molecular targets against HL60 cells.

Results: The results demonstrated that SA was governed by nanoformulations under the dual–trigger release of pH/glutathione, and it typically fit the Korsmeyer–Peppas kinetic model. The nanoformulations enhanced the anticancer effect against HepG2 cells and HL60 cells compared to SA but were less cytotoxic to MRC5 normal cells and regulated various molecular pathways of apoptosis. Most importantly, new results were obtained on the genetic regulation principle through the high inhibition of long noncoding RNAs (HOTAIR, HULC, CCAT1, and H19) and matrix metalloproteinases (MMP–2 and MMP–9), providing a novel leukemia target.

Conclusions: These results suggest potential impacts for nanoformulations composed of SA with a sustained release pattern controlled by dual–trigger release of pH/GSH that enhanced anticancer cells. This approach may offer a new route for using EOs as new targets for cancers and open the door for deep preclinical investigations.

Keywords: Anti-leukemia cancer targeting, Natural agent-drug delivery system, Dual-trigger release of oil, Mesoporous silica nanoparticles, *Satureja hortensis* essential oil, Long noncoding RNAs, Matrix metalloproteinases

Background

Cancer remains one of the major causes of death with a considerable negative impact on the health care infrastructure, costs of medical care, and lifestyle. In addition, either no curative treatments are available or expensive costs for some cancers. In particular, leukemia, a hematologic malignancy, is largely detected in adults and affects the bone marrow, lymphatic system, and blood cells. (Siegel et al. 2016) There are several types of leukemia, including chronic myeloid leukemia (CML), acute lymphocytic leukemia (ALL), chronic lymphocytic leukemia (CLL), and acute myeloid leukemia (AML). AML is the most common form of leukemia in adults, and chemotherapy or the transplantation of allogeneic stem cells are the main treatments (Farge et al. 2017; Guamán-Ortiz et al. 2017). Chemotherapy is associated with high cost, toxicity, and cancer resistance (Estey 2018). Thus, two strategies have recently been explored for targeting AML. In one scenario, an alternative to chemotherapy, screening natural agents for new antileukemia has prompted the search for safe and low–cost therapy (Siveen et al. 2017). In this connection, a very recent study by (Bouhtit et al. 2021) demonstrated that the combination of carvacrol and thymol, components present in many essential oils, shows effective synergistic effects against AML cells. Additionally, (Hsiao et al. 2020) showed that curcumin and its analog induce apoptotic cell death in AML cells. Of interest, in the current research, essential oils (EOs) are biologically active natural agents characterized by distinguished odor, volatile, oily liquids produced by medicinal and aromatic plants. EOs are obtained from plants and possess various pharmacological and anticancer activities. The challenge in their application is low stability, high volatility, and high risk of deterioration by exposing them to direct heat, humidity, light, or oxygen. Nanomedicine formulations can overcome these challenges (Watkins et al. 2015; Aljuffali et al. 2016; Fonseca-Santos and Chorilli 2020; AbouAitah et al. 2018; Shahein et al. 2019; Lammari et al. 2020; Froiio et al. 2019; Attallah et al. 2020; de Matos et al. 2019). In the second scenario, emerging research for AML therapy is developing a drug delivery system (DDS) mainly to control drug release, increase targetability, reduce toxicity, and improve therapeutic efficacy. Here, few designs are examples of DDSs for AML (Zhou et al. 2017) developed a pH-sensitive controlled DDS made of doxorubicin-loaded functionalized mesoporous silica nanoparticles conjugated to rituximab for active targeting, improving the activity and reducing the side effects in cells. Yasinska et al. 2018 constructed efficient delivery for AML cells using gold nanoparticles conjugated with rapamycin through a glutathione linker. Furthermore, (Shao et al. 2019) designed a codelivery employing a lipid-polymer hybrid nanoparticle as a core loaded with doxorubicin and gallic acid and surface modified with hyaluronic acid, which showed high targetability and efficiency against AML cells.

In our previous DDSs for targeting cancers, mesoporous silica nanoparticles (MSNs) were used as a nanocarrier for anticancer natural agents: colchicine for HCT116 colon cancer cells (AbouAitah et al. 2020a), thymoquinone for brain cancers (Shahein et al. 2019), and curcumin for HepG2 liver cancer cells (AbouAitah et al. 2018). MSNs are one of the most commonly used drug carriers because they have unique characteristics ideal for DDSs: good biocompatibility, high stability, high surface area, high loading capacity, easy surface functionalization, controlled drug release and others (Tang et al. 2012; Ashley et al. 2011; Slowing et al. 2008; Li et al. 2014; Li et al. 2016; Jermy et al. 2021).
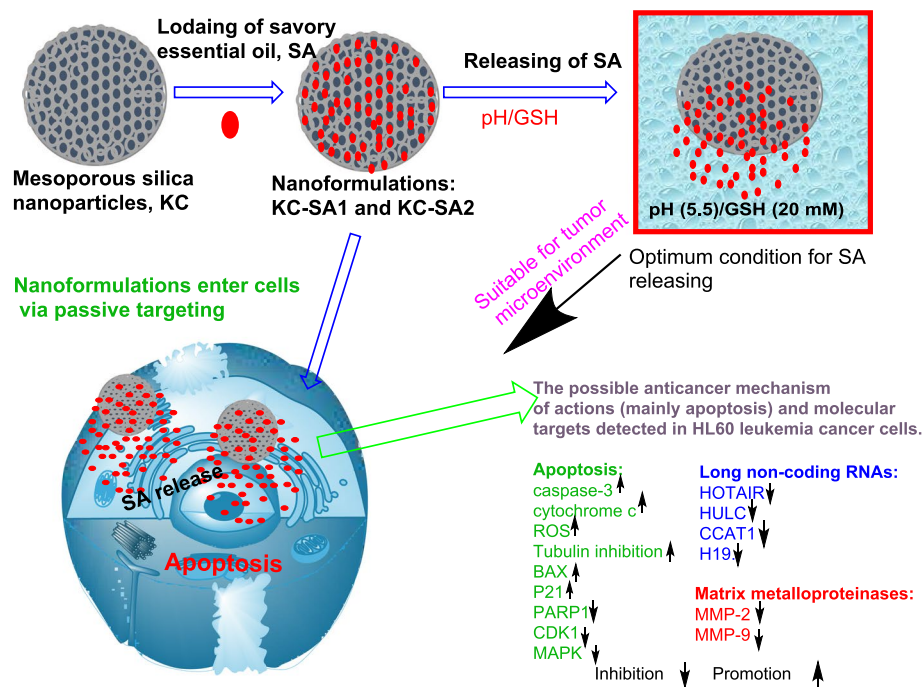
Scheme 1 Preparation of nanoformulations and a dual–trigger release of SA under pH/GSH. Illustration of SA releases into HL60 cells and possible mechanism of actions along with molecular targets especially lncRNAs and MMPs and their expression/level status detected in cells compared to control HL60 cells without treatments

In the current study, we introduce a novel delivery system depending on nanoformulation prototypes using MSNs for summer savory essential oil (SA) obtained from the *Satureja hortensis plant* (Scheme 1). The SA contains many components, mainly carvacrol up to ~47%, γ-terpinene up to ~39%, and other minor components, including α-thujene (~1%), α-pinene (~1.8%), α-terpinene (~2.8%), ρ-cymene (~4%), and terpinolene (~2.6%). (El-Leithy et al. 2017) Only a few studies have shown the anticancer potential of SA, such as melanoma cell lines (Popovici et al. 2019) and breast cancer cells and chronic myeloid leukemia (Ahmadi et al. 2021). To our knowledge, no nanoformulations have been published for SA or other EOs with MSNs concerning cancer therapy, including AML. We intended to evaluate whether the nanoformulations can control SA under internal stimuli-responsive conditions of pH/GSH; whether the nanoformulations can enhance the anticancer activity over SA; the possible mechanism of action; and finally, whether the nanoformulations can modulate genetic regulation: long noncoding RNAs (lncRNAs) and matrix metalloproteinases (MMPs). We obtained new results, especially for lncRNA and MMP evaluation, which could serve as new leukemia targets.

Materials and methods

Materials

The SA EO was extracted by the stem distillation method according to El–Leithy (El-Leithy et al. 2017). The EO was collected and used in our studies. Tetraethyl orthosilicate, cetylpyridinium bromide (CPB), cyclohexane, isopropanol, and urea were purchased from Sigma–Aldrich (St. Louis, MO, USA). Ethanol and methanol were obtained from

Thermo Fisher Scientific, Loughborough, UK. Dimethyl sulfoxide (DMSO) was purchased from Tedia, Fairfield, OH, USA. Phosphate-buffered saline (PBS) and glutathione (GSH) were purchased from Acros Organics, Geel, Belgium. DMEM (Dulbecco's modified Eagle's medium), RPMI 1640 medium, and fetal bovine serum (FBS) were obtained from Gibco/Life Technologies, Thermo Fisher Scientific-Langenselbold, Germany. Insulin from Novo Nordisk, Bagsvaerd, Denmark. Penicillin G, streptomycin, and MTT assay kits were obtained from Sigma–Aldrich, St. Louis, USA. The tissue culture plates were obtained from Greiner Bio-One GmbH (Frickenhausen, Germany). A Caspase-3 (active) Human ELISA kit from Invitrogen (Cat. KHO1091, Camarillo, CA, USA); ELISA kit for tubulinβ assay (TUBb, SEB870Hu, Cloud-Clone Corp., Houston, TX, USA); human Bax ELISA kit (XXDRG, USA); human Bcl2 ELISA kit (Zymed, Cat. no. 99-0042, Carlsbad); human cytochrome c ELISA kit (Abcam, Vienna, Austria); ELISA Cleaved PARP kit (Invitrogen, Cat. KHO0741, Camarillo, CA, USA); ROS ELISA Kit (EIAab, Cat no: E1924r, Wuhan, China); Script One-Step RT–PCR Kit with SYBR® Green from BIO-RAD (Hercules, CA, USA); miRNeasy extraction (Qiagen, Valencia, CA, USA); human matrix metalloprotein 2 (MMP-2) ELISA kit (Wkea Med Supplies Corp, Changhun, China); human matrix metalloprotein 9 (MMP 9) platinum ELISA (Affymetrix eBioscience, Cat. BMS2016/2 and BMS2016/2TEN, Vienna, Austria). All chemicals, reagents, and solvents used in our study were of analytical grade.

Methods

Synthesis of mesoporous silica nanoparticles and essential oil loading

Mesoporous silica nanospheres of three-dimensional type were synthesized according to our previous method reported by (AbouAitah et al. 2018). The prepared silica nanospheres were named KC. SA loading was performed by adding silica nanospheres (500 mg) in ethanol (Thermo Fisher Scientific, fLoughborough, UK) containing two concentrations of SA. The solution was stirred at room temperature for 24 h, recovered, washed two times, and freeze-dried for further use. Two materials were prepared based on the additional amount of SA to KC used. The resulting materials were named KC–SA1 (for using high SA concentration) and KC–SA2 (for using low SA concentration).

Characterization techniques

In our study, we characterized the materials with several techniques to verify their physicochemical properties. Field emission scanning electron microscopy (FE-SEM; Ultra Plus, Zeiss, Jena, Germany) was used to observe the morphology of the prepared silica nanospheres. The specific surface and mesoporosity characteristics of nanospheres before and after loading were measured using a NOVA automated gas sorption system (NOVA, Quanta Chrome Instruments, Florida, USA). For this purpose, the nanoparticles were degassed (overnight at 50 °C) before analysis. We used Fourier transform infrared (FTIR) spectroscopy (Bruker Optics Tensor 27, Bruker Corporation, Billerica, MA, USA) to identify changes in the surface-functional group following SA loading. The thermal properties and the crystalline state of SA loaded to materials were detected by gravimetric analysis coupled to differential scanning calorimetry (TGA–DSC, Shimadzu TGA–DSC 50, Shimadzu, Kyoto, Japan). The conditions of the measurements were as follows: the temperature was programmed to reach 800 °C, and the heating rate

was 10 °C/min under a nitrogen atmosphere. The XRD patterns of the materials were obtained by an XRD system (PANalytical, Henderson, NV, USA) employing CuKα radiation (at 45 kV voltage and 40 mA current) in the 2θ range from 5 to 100°. Zeta potential and size analysis (employing dynamic light scattering) measurements were performed for a water suspension of nanoparticles using a Malvern ZetaSizer (NanoZS, Malvern Instruments Ltd., Malvern, UK).

Entrapment efficiency and total drug content characteristics

For the entrapment efficiency (EE), KC-SA1 or KC-SA2 (10 mg) was dissolved in 10 mL ethanol under stirring for 2 h (to ensure high extraction); subsequently, the sample was centrifuged with a high-speed cooling centrifuge (at 25,000 rpm) for 30 min at 4 °C (Sigma 3–30 KS, Sigma Laborzentrifugen GmbH, Osterode am Harz, Germany). Next, the supernatant was collected and used to determine the EE spectrophotometrically by a UV–Vis spectrophotometer (Shimadzu UV spectrophotometer (240 j/PC), Japan) at 390 nm. The following equations were applied to calculate EE% according to our previous report:

$$
\begin{aligned}
\text{EE (\%)} = &\ \text{Initial amount of SA theoretically calculated} \\
& - \text{Amount of free SA actually measured in supernatant} \\
& /\text{Initial amount of SA theoretically calculated}
\end{aligned}
\tag{1}
$$

For the determination of total drug content and total drug capacity, 10 mg of KC-SA1 or KC-SA2 was dissolved in ethanol (10 mL) under vigorous stirring for 4 h and then filtered by a syringe filter with a 0.2 μm filter to prevent any silica mesosphere particles from entering the solution. Finally, the concentration of SA was determined by measuring the absorbance at nm. Both loading capacity and total content% were calculated based on these equations:

$$
\text{Total loading content (\%)} = \text{Amount of SA entrapped/weight of KC} * 100
\tag{2}
$$

$$
\begin{aligned}
\text{Total loading capacity (\%)} \\
= \text{Experimental content of SA} \\
/\text{theoretical content of SA in KC particles} * 100
\end{aligned}
\tag{3}
$$

Solubility experiment protocol

The SA solubility was determined according to a previous study (Ammar et al. 2013). In 50 mL glass bottles, 1 mL of SA was allowed to dissolve at 37 ± 0.5 °C in 5 mL of each of the following ($n=3$): PBS at three different pH values (7.4, 6.8, and 5.5) with and without GSH and absolute ethanol. Samples were kept under continuous shaking in a shaking incubator (GFL 3032, Gesellschaft fur Labortechnik GmbH, Burgwedel, Germany) at 150 rpm. Samples were checked for complete solubility every 24 h. Wherever solubility was observed, another 1 mL of the SA was added to the solvent solution. The process was repeated daily until no further solubility was possible. At this point, saturation is achieved. Thus, samples were centrifuged at 5000 rpm for 5 min at room temperature using a table-top centrifuge (Sigma 3-30KS, Sigma Laborzentrifugen GmbH, Osterode

am Harz, Germany). The upper oil layer was separated, while the remaining solution was analyzed for SA dissolved using a UV–Vis spectrometer (Shimadzu UV spectrophotometer (240 j/PC), Japan). The solubility measurements were repeated three times.

In vitro release studies

We carried out the in vitro release in release media of different pH values according to our previous method (AbouAitah et al. 2020a, b, 2021). These were PBS at three different pH values: pH 7.4, 6.8, and 5.5. In addition, 10 mM and 20 mM GSH were independently added to each of the previous PBS media, mimicking the tumor environment. Briefly, 5 mg of KC-SA1 or KC-SA2 was accurately weighed and placed in a cellulose dialysis bag (MWCO 12,000 g/mol, Sigma–Aldrich CHEMIE GmbH, Sternheim, Germany) containing 3 mL of the corresponding release medium. Each bag was then tightly closed from both ends and immersed in a capped glass bottle containing 50 mL of the release medium. Samples were shaken at 150 rpm at 37 °C in a shaking incubator (GFL 3032, Gesellschaft fur LabortechnichmbH, Burgwedel, Germany). At predetermined time intervals (from 1 to 15 days), a 2 mL aliquot of the release medium was withdrawn and replaced with the same volume of fresh medium. Thereafter, samples were analyzed for the released amount of SA at the corresponding wavelength of maximum absorbance using a UV–Vis spectrophotometer. The mean cumulative percent of the oil released was calculated from triplicates at each time interval. Finally, the obtained release data were kinetically analyzed (KineDS3 software, Jagiellonian University, Krakow, Poland) with different kinetic models, either linear or nonlinear regression.

In vitro cytotoxicity evaluation

Cell cultures   In our study, two cancer cell lines, HepG2 human hepatic carcinoma (ATCC® HB-8065TM) and HL60 leukemia cancer (ATCC® CCL-240™), and MRC5 human lung fibroblast cells (ATCC® CCL-171™), employed as normal cells were investigated. The cells were from VACSERA, Dokki, Giza, Egypt, where some assays were performed. All cells were cultured in Dulbecco's modified Eagle's medium (DMEM) supplemented with 10% FBS, penicillin G (100 U/mL), and streptomycin (100 μg/mL) and maintained at 37 °C in a humidified 5% CO_2 atmosphere.

In vitro cytotoxicity assessment

We assessed the anticancer effect utilizing the 3-4,5-dimethylthiazol-Z-yl-2,5-diphenyltetrazolium bromide (MTT) assay described in detail in our previous study (Shahein et al. 2019). To evaluate the cytotoxicity of MSNs, all cells were treated at 0.1, 1, 10, 100, and 1000 μg/mL. To evaluate the anticancer activity of SA, KC-SA1, KC-SA2, and staurosporine (STS), we used them at concentrations of 0.01, 0.1, 1, 10 and 100 μg/mL in PBS buffer. Nanoformulations containing SA were used in equivalent amounts to SA. For comparison, 100 μL of PBS was used in the control. Furthermore, after all treatments, the cells were incubated for 48 h. After each incubation period, the media were removed, and fresh DMEM containing 50 μL of MTT solution (1 mg/mL) was added to each well. Then, the cells were incubated for an additional 4 h at 37 °C. Next, the medium containing MTT solution was discarded, and 100 μL of DMSO was applied and shaken. Finally, the absorbance was read at 540 nm by an ELISA reader (Robonik P2000

AbouAitah *et al. Cancer Nanotechnology* (2023) 14:3

Page 7 of 32

ELISA, India PVT LTD, Thane, India). The MTT assay was performed in triplicate, and the obtained data are expressed as the mean $\pm$ standard deviation (SD).

Caspase-3 activity assessment

Caspase-3 activity was measured according to detailed procedures previously reported in our study (Shahein et al. 2019). Briefly, HL 60 cells were cultured (on 96-well plates) to reach a density of $1.2–1.8 \times 10,000$ cells per well, containing 100 μL of complete growth medium (RPMI 1640) supplemented with 10% FBS, and grown at 37 °C. Afterward, the cells were treated with 100 μL of the tested sample (at IC50) of KC, KC-SA1, KC-SA2, and SA in each well and incubated for 48 h before the assay assessment. For the control, HL60 cells received only PBS. Thereafter, the cells were lysed using cell extraction buffer. Subsequently, the lysates were diluted by adding the standard dilution buffer to obtain a proper range for determining the human active caspase-3 content. Finally, the absorbance was recorded at 450 nm using a Robonik P2000 ELISA reader. Each sample was analyzed in triplicate, and the data are expressed as the mean $\pm$ SD.

Tubulin inhibition activity assessment

We assessed tubulin polymerization using an ELISA kit (TUBb (SEB870Hu, Cloud-Clone Corp., Houston, TX, USA) based on the manufacturer's instructions and detailed procedures according to our previous report. (AbouAitah et al. 2020a) HL60 cells were cultured in 96-well plates at a cell density of $1.2–1.8 \times 10,000$ cells per well containing 100 μL of MEM growth medium. Subsequently, the cells were incubated with nanoformulations, SA, and STS at IC50 (μg/mL) concentrations for 48 h; for the control, HL60 cells received only PBS. Then, the solution was removed, the cells were detached by trypsinization, washed with cold PBS buffer, suspended in PBS, and lysed with three freeze/thaw cycles. Following these steps, cell lysates were centrifuged for 10 min (using a cooling centrifuge). The detection assay was performed with further steps as instructed in the manufacturing kit. Samples were finally used to measure color at 450 nm by an ELISA reader (Robonik P2000). The experiments were performed in triplicate, and the data were calculated as percent inhibition.

Bax and Bcl$_2$ assessment

Bax and Bcl$_2$ levels were determined by ELISA using cell lysates according to the manufacturer's protocols. For Bax, a human Bax ELISA kit (DRG, USA) was used, whereas for Bcl$_2$, a human Bcl2 ELISA kit (Zymed, Cat. no. 99–0042, Carlsbad) was used. The HL60 cells were treated at the IC50 of different samples and incubated for 48 h. HL60 cells without any treatments were used as a negative control. The cells were lysed and assessed according to the ELISA kit instructions. The Bax protein and Bcl$_2$ levels were determined by measuring the absorbance at 450 nm with a Robonik P2000 ELISA plate reader. The samples were analyzed in triplicate.

Cytochrome c assay

To assess cytochrome c accumulation in HL60 cells, we used a cytochrome c ELISA kit depending on the cell lysates according to the manufacturer's protocol from Abcam (Abcam, Austria). The HL60 cells were plated at a density of $1.2–1.8 \times 10,000$ cells per

well and treated with the IC50 concentration of each sample and incubated for 48 h. After several steps were procured, the absorbance was detected at 450 nm with a Robonik P2000 microplate reader. Each sample was made in triplicate.

PARP-1 enzyme assessment

PARP-1 was assessed depending on the cell lysates using the ELISA Cleaved PARP kit from Invitrogen (Cat. KHO0741, Camarillo, CA, USA). To obtain lysates from treated and untreated control cells, HL60 cells were seeded at a density of $1.2–1.8 \times 10,000$ cells per well treated at the IC50 (µg/mL) of various samples used in our studies and incubated for an additional 48 h. The cells were lysed and assessed according to the ELISA kit instructions, and the absorbance of the samples was measured at 450 nm by a Robonik P2000 ELISA plate reader. In addition, the samples were analyzed in triplicate.

ROS assessment

To evaluate the intracellular expression of ROS in HL60 cancer cells**,** we used an ROSELISA Kit (EIAab, cat no: E1924r, Wuhan, China) according to the manufacturer's instructions. Briefly, after treatment and incubation of HL60 cells, all samples used in our studies at their IC50s (control cells received no treatments), they were harvested, homogenized, and centrifuged, and the clear supernatant was obtained for colorimetric assay measurements. Then, various steps were performed following the instructions for the ROS assay, and finally, the absorbance of the samples was measured by a microplate reader at 450 nm (Robonik P2000 ELISA reader). Each tested sample was analyzed in triplicate.

Measurement of CDK1 and P21 expression

Cell culture treatment and RNA extraction   Initially, HL60 cells were grown in cultured plates at a density of 1×10^6 and then treated with the IC50 concentration (µg/mL) of each nanoformulation, free SA, and STS incubated for 48 h. For RNA extraction, cells were collected and extracted with a RNeasy extraction kit according to the manufacturer's protocol (Qiagen, Hilden, Germany). Then, the cells were disrupted in RLT buffer, homogenized, and disrupted before ethanol was added to the lysates. Then, 100 µL of sample lysate was added to a RNeasy Mini spin column with total RNA binding to the membrane. To elute the high-quality RNA, RNase-free water was used. During all steps of binding, washing, and elution, centrifugation with a microcentrifuge was employed.

Quantitative determination by RT–PCR   To detect CDK1 and p21 expression, a real-time polymerase chain reaction (RT–PCR) technique was used with the BIORAD iScriptTM One-Step RT–PCR Kit with SYBR® Green (Bio–Rad, Hercules, CA) following the manufacturer's protocol. The following primers were used in our study: for the CDK1, p21, and β-actin genes: CDK1 F, 5′-A T G A A G A AAA T T C G A T TG G A A A A C G -3′; CDK1 R, 5′-G A T C T C C G A G G A G G A C C T G A A C TAA-3′; p21 F, 5′- GAGGCCGGG ATGAGTTGGGAGGAG -3'; and p21R5'-CAGCCGGCGTTTGGAGTGGTAGAA-3'.; β-actinF, 5′ GTGACATCCACACCCAGAGG-3'; and β-actin R 5′-ACAGGATGTCAA AACTGCCC-3'. The reactions were performed in triplicate (using a Rotor-Gene 3000 RT–PCR system) and analyzed by Rotor-Gene Series Software 1.7 (Build 87).

Assays for HOTAIR, CCAT, HULC, H19, MMP-2 and MMP-9

Cell culture and treatment   HL60 leukemia cancer cells were seeded in 96-well plates at a density of $1.2–1.8 \times 10{,}000$ cells per RPMI 1640 medium (supplemented with 10% FBS, 10 μg/mL insulin, and 1% penicillin-streptomycin) and grown for 24 h. As in the other assays mentioned above, we used KC, KC-SA1, KC-SA2, SA, and STS at their IC50 concentrations (μg/ml) and incubated them for 48 h. For comparison, HL60 cells were left untreated with any samples. As the supernatants are the main part to be used for assays, we prepared the cell culture supernatants according to (AbouAitah et al. 2020a). The supernatant lysates were used for the determination of the expression levels of HOTAIR, CCAT, HULC, H19, MMP–2, and MMP–9 through RT–PCR or ELISA.

To measure human matrix metalloprotein 2 (MMP-2) and human matrix metalloprotein 9 (MMP 9), ELISA was employed using an ELISA plate reader (Model stat fax 2100, Awareness, Ramsey, MN, USA). The protocols were performed according to the manufacturer's instructions for each assay. To measure long noncoding RNAs (lncRNAs) (HOTAIR, CCAT, HULC, and H19), RNA was extracted. According to the manufacturer's instructions from the miRNeasy extraction kit (Qiagen, Valencia CA, USA) and QIAzol lysis reagent, total RNA, including lncRNAs, was extracted from the prepared supernatants. Furthermore, the concentration of RNA through our studies was determined using a NanoDrop2000 (NanoDrop2000, Thermo Scientific, Wilmington, NC, USA), permitting a high accuracy for measuring any small quantities of RNA. For reverse transcription, 20 μL of the extracted RNA was analyzed using the RT2 First Strand kit (Qiagen) according to the manufacturer's instructions. To identify the expression levels of lncRNAs, GAPDH is usually used as an internal control for serum lncRNAs (Shaker et al. 2017; Duan et al. 2016) according to the manufacturer's protocol. The HOTAIR, CCAT, HULC, and H19 Ref Seq no. was NR 002819.2. lncRBase accession numbers (Gene Globe IDs). The primer sequences for GAPDH were 5′-CCCTTCATTGACCTC AACTA-3′ (forward) and 5′-TGGAAGATGGTGAT GGGATT-3′ (reverse). The RT–PCR assay was carried out in a 20 Ml reaction mixture with the Rotor gene Q System (ROTOR-Gene Q, SN R1211164, Qiagen, Hilden, Germany). The following conditions were studied: 95 °C for 10 min, followed by 45 cycles at 95 °C for 15 s and 60 °C for 60 s. To quantify the target genes relative to their endogenous control, the cycle threshold (Ct) method was followed. Concerning the lncRNAs, the ΔCt of lncRNAs was calculated by subtracting the Ct value of GAPDH from those of HOTAIR, CCAT, HULC, and H19. The expression levels were expressed as the fold change for lncRNAs (HOTAIR, CCAT, HULC, and H19), calculated using the Eq. 2-ΔΔCt. Additionally, gene expression was calculated relative to the internal control (2-Ct), and the fold change was also calculated using 2-Ct for relative quantitation (Livak and Schmittgen 2001).

Statistical analysis

Data for biological evaluations are expressed as the mean ± SD. Significance differences were calculated using the t test and analysis of variance (ANOVA) at $p < 0.05$, and the calculations were performed by GraphPad PRISM (Version 8.0.1, GraphPad Software, San Die-go, CA, USA).
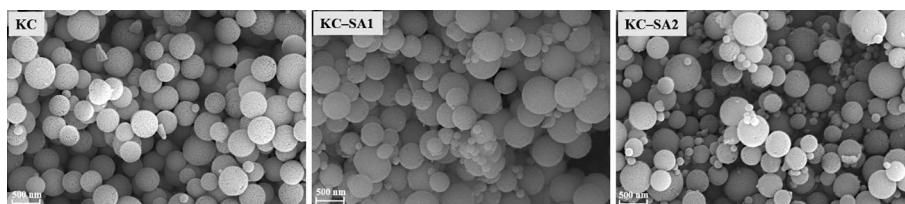
Fig. 1 Field emission scanning electron microscopy (FE-SEM) images of KC nanospheres and nanoformulations (KC–SA1 and KC–SA2). No considerable difference was observed before and after SA loading

Table 1 Physicochemical and loading properties of materials

Material	S_{BET} (m^2/g)[a]	Total pore volume[b] (cm^3/g)	Mean pore size diamter[c] (nm)	Weight loss wt.%[d]
KC	297	0.358	4.81	11.14
KC–SA1	100	0.190	7.54	41.60
KC–SA2	75.3	0.142	7.54	30.84

[a] The specific surface obtained from adsorption–desorption measurements

[b, c] The pore volume and pore size distribution of materials by means of the Brunauer-Emerett-Teller

[d] The weight loss property obtained by the thermogravimetry measurement from RT to 1000 °C

Results and discussion

Material characterization and physicochemical properties

Physicochemical properties of the materials

Figure 1 shows no changes in the morphological structure of KC spheres before and after SA loading, as indicated by SEM images, which is expected. Table 1 lists the specific surface area, pore characteristics, and TGA thermal analysis before and after SA loading in nanoformulations. The KC showed the highest surface area (297 m^2/g) and total pore volume (0.358 cm^3/g), whereas it recorded the lowest values for pore diameter and weight loss properties of 4.81 nm and 11.14 wt.%, respectively. One can see an almost simultaneous decrease in the mass of the sample, falling below 3 wt.%. The results display a considerable change in the physicochemical properties after SA loading, decreasing the surface area and pore volume while increasing the pore diameter and weight loss characteristics. The surface area reached 75.3 m^2/g, and the pore volume was 0.142 cm^3/g for KC-SA2. The pore size distribution did not differ between nanoformulations, but KC-SA1 showed a greater weight loss of up to 41.6 wt.% than KC-SA2. This observation may be related to the highest SA loading content. The observation that pore size dimeters were larger in nanoformulations compared to KC may be associated with the SA filling the small pores in KC than large pores. The results (Fig. 2A, B and C) indicated that the decomposition behavior of the materials was characterized by different steps for KC and nanoformulations. For the nanoformulations, initially, the mass loss was due to the removal of the water content of the materials (at ~100 °C), and the next stage appeared from 100 °C to ~630 °C, connected with the decomposition of SA. The last stage observed up to 1000 °C, with no practical mass change, may be related to KC. These results for the nanoformulations containing SA are in line with previously
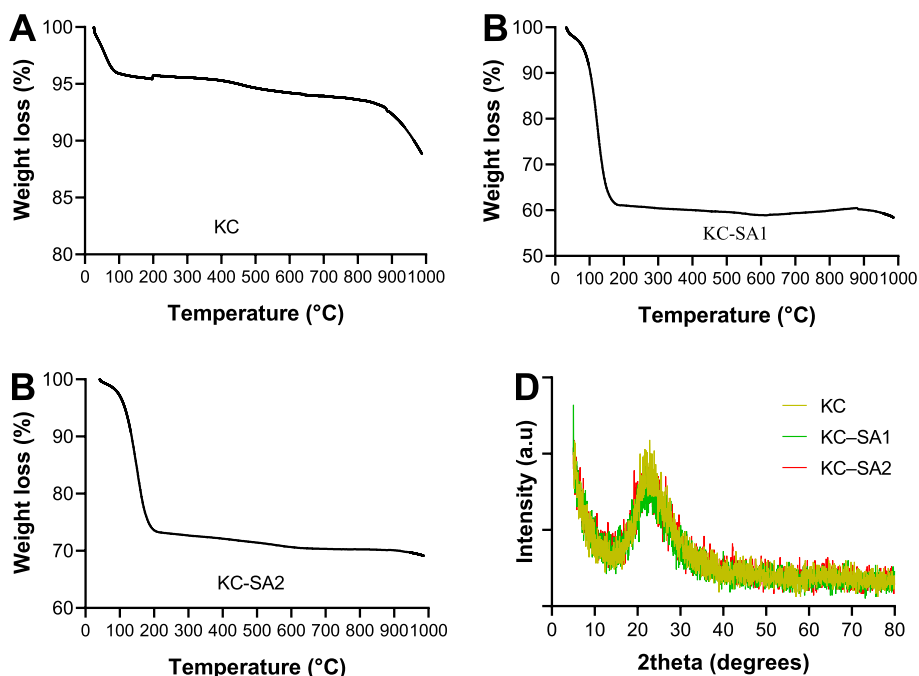
Fig. 2 The simultaneous thermal (STA) and X-ray diffraction (XRD) analyses for materials before and after SA loading. STA analysis for KC (**A**), KC–SA1 (**B**), and KC–SA2 (**C**). The XRD analysis for materials before and after SA loading (**D**)
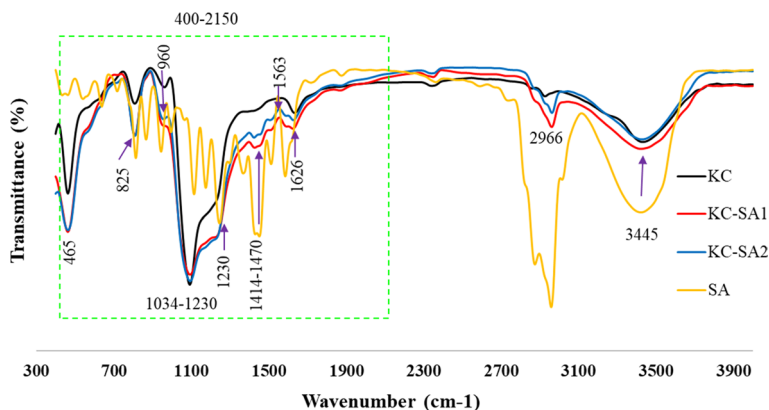
Fig. 3 Fourier transform infrared spectroscopy (FTIR) spectra were obtained for all materials before and after SA loading

published studies employing MSNs for carrying essential oils (Melendez-Rodriguez et al. 2019; Sattary, Amini, and Hallaj 2020).

XRD measurement

Figure 2D shows no obvious differences before and after SA loading to MSNs. Only a small shift of the diffraction peaks was observed. The obtained results agree with previous data for loading thymol into SBA-15 (Gámez et al. 2020; Xie and Zhang 2016). This observation can be ascribed to the presence of most SA in the pores of MSNs.

FTIR analysis

As indicated by Fig. 3, the FTIR spectra detected for KC, nanoformulations, and SA showed new peaks in nanoformulations regarding SA compared to KC. In the KC spectrum, several bands were detected at 465, 825, 1095, and 3434 cm^{-1}, confirming the siliceous mesostructured silica nanospheres (AbouAitah et al. 2016, 2018, 2020a). The main changes in the nanoformulation spectra compared to the KC spectrum were observed at 400–2150 cm^{-1}. Both nanoformulations spectra demonstrated intense peaks that were detected at 465, 825, 960, and 1626 cm^{-1}, arising from the major bands of SA. In this region, also observed in nanoformulations, a broad shifted peak at 1034–1230 cm^{-1} and a new peak at 1563 cm^{-1} were attributed to SA bands in this region. A distinguishing new peak for nanoformulations was obtained in the region centered at 2966 cm^{-1}, indicating the presence of SA. A peak centered at 3445 cm^{-1} for KC-SA1 was associated with the stretching vibrations in the region from 3100 cm^{-1} to 3700 cm^{-1}. The FTIR results for nanoformulations provide evidence for the presence of SA in nanoformulations. Additionally, FTIR results indicated that SA, even at a small fraction, may still be attached to the surface of KC nanoparticles. The obtained FTIR data for nanoformulations are consistent with previous studies concerning the loading of natural agents to MSNs (Shahein et al. 2019; AbouAitah et al. 2018).

Size and zeta potential measurements

Table 2 depicts the significant differences between both nanoformulations as indicated by their particle size and zeta potential characteristics. KC-SA2 had a larger mean particle size (~400 nm) than KC-SA1 (~330 nm), but the later nanoformulation recorded a higher negative zeta potential (~42 m/V) than KC-SA2 (~36 m/V). The plausible reason for this observation can be attributed to the difference in the SA amount in nanoformulations. These results not only indicate that the particle size obtained for nanoformulations is considerable for cellular uptake by cells but also demonstrate the stability of particle size in dispersion. Widely, the particle size property of particles determines the method of intracellular uptake and internalization in cells, e.g., nonphagocytosis (He et al. 2010) (particle size up to 50 nm), pinocytosis, including clathrin-mediated endocytosis and caveolin-mediated endocytosis (Doherty and McMahon 2009; McMahon and Boucrot 2011; Sahay et al. 2010) (particle size from 150 to 200 nm), and macropinocytosis and phagocytosis (Foroozandeh and Aziz 2018) (particle size of 250 nm to 3 µm). Additionally, nanoparticles with high values (negative or positive zeta potential) are electrically and physically stable due to the repulsion force between adjacent particles in the

Table 2 The particle size and zeta potential measurements of nanoformulations

Formula	Mean particle size (nm)[a]	Zeta potential (m/V)[b]
KCC-SA1	330 ± 80	−42 ± 2.6
KCC-SA2	396.6 ± 86.2	−36 ± 2.5

[a] The particle size measurement of the nanoformulations was performed for the aqueous solution of each material in deionized water through the DLS method at RT

[b] The zeta potential analysis was investigated for the aqueous solution of nanoformulations dispersed in deionized water, measuring by Zetasizer technique at RT. The statistical analysis using t-test at $p < 0.05$ shows the significant differences between nanoformulations for particle size (p-value was 0.017; *) and zeta potential analysis (p-value was 0.006; **)

Table 3 SA loading and efficiency properties

Formula	Total content (TC)	Loading capacity (LC)	Entrapment efficiency (EE)
KCC-SA1	52.25 ± 3.07	48.10 ± 2.13	96.05 ± 4.88
KCC-SA2	32.19 ± 1.66	30.29 ± 2.94	80.71 ± 2.62

solution, indicating good stability. (Frank et al. 2020). The optimum values that are sufficient to induce the repulsive force should be > -30 mV to $+30$ m/V (Joseph and Singhvi 2019), as well as from -41 to -50 m/V (Losso et al. 2005). From the obtained results, the prepared nanoformulations reveal good stability in liquid solution.

SA loading properties

The UV–Vis results in Table 3 display the successful loading of SA into MSNs with high loading capacity and efficiency for nanoformulations. From the TDC and LC data, the maximum TDL ($\sim$ 51%) and LC ($\sim$ 48%) were in KC–SA1 compared to KC–SA2. This result can be explained by the increase in the initial amount of SA used during the preparation. The SA:MSN ratio was higher for KC–SA1 (1:1) than KC–SA2 (1:1.5). Both TDC and LC parameters show the potential of MSNs as proper nanocarriers for EOs, as indicated by SA. In this connection, the SA loading efficiency reached $\sim$ 97% as in KC–SA1. To the best of our knowledge, these results, especially those of TLC, have not yet been achieved by other nanoformulations formulated by different nanocarriers when a crude essential oil contains complex compounds. For instance, the loading capacity reported for jasmine in pectin/chitosan nanoparticles ($\sim$ 6%) (Attallah et al. 2020), zedory in chitosan-grafted MSNs ($\sim$ 41%) (Jia et al. 2019), peppermint & green tea in chitosan nanoparticles ($\sim$ 23%) (Shetta et al. 2019) and savory in alginate microparticles ($\sim$ 26%) (Hosseini et al. 2013). Alternatively, to use crude EOs, loading of single separated components into MSNs is another and easier approach. As MSNs are considered nanocarriers for them, only a few systems have been reported. Melendez-Rodriguez et al. 2019 for the efficient incorporation of eugenol into MSNs up to 50 wt.%, used as antibacterial film application.

The solubility property

As Additional file 1: Table S1 indicates, the SA solubility varied between the three tested media of ethanol, PBS at different pH values, and PBS–combined GSH adjusted to pH values. The solubility increased with ethanol (0.2 mg/mL) compared to PBS alone, even adjusted from low acidic to neutral physiological pH, as expected. When PBS contained GSH (20 mM), specifically at low acidic pH (5.5), SA solubility was enhanced to 0.3 mg/mL. These results demonstrate that the solubility of SA can be modulated from low to enhanced under specific conditions. This modulation is of great importance for drug delivery systems for cancers because the tumor environment is characterized by high GSH (Bansal and Simon 2018) and low acidic pH (Feng et al. 2018).
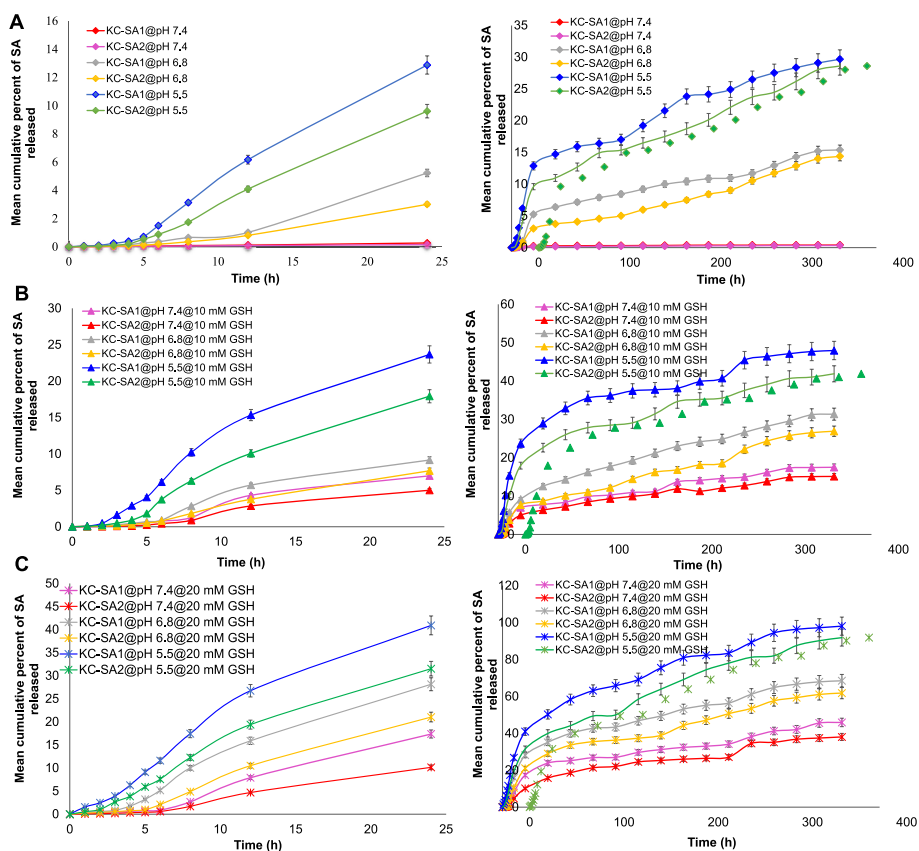
Fig. 4 In vitro mean the cumulative release of SA profiles under different conditions of pH and GSH (glutathione). SA release from nanoformulations under three levels of pH (7.4, 6.8, and 5.5) (**A**). SA release from nanoformulations under three levels of pH (7.4, 6.8, and 5.5) combined with GSH (10 mM) (**B**). SA release from nanoformulations under three levels of pH (7.4, 6.8, and 5.5) combined with GSH (20 mM) (**C**). The data presented for release profiles are mean ± SD

In vitro release kinetics

As proof of SA release and kinetics from MSNs used to build nanoformulations, we tested the release under different pH levels and GSH concentrations. As Fig. 4 shows, SA was released from the nanoformulations with sustained long-term release over 15 days. To better present the release behaviors, we showed the release pattern within 24 h and then the full pattern within 15 days. As a general note, the release results followed the solubility profile of SA in various release media (Additional file 1: Table S1), where the pH combined with GSH as a dual-trigger release was the limiting factor for controlling SA release from nanoformulations.

Figure 4 shows the cumulative release under conditions adjusted only to pH 7.4, 6.8, and 5.5. Within 24 h, no burst release effect was seen up to ~6 h, and the maximum release was found to be ~13% for KC–SA1 under low acidity conditions (pH 5.5) compared to another release at pH 7.4 and 6.8. Further extending the release time to 15 days, a higher cumulative release percent obtained for KC–SA1 and KC–SA2 reached nearly 30% at pH 5.5, followed by the release at 6.8 (~15%) and 7.5 (minimum release percentages, 0.5%). It can be seen from these data that almost no release occurred. This observation confirms that the release of SA is controlled by pH. In the next stage of the

experiments, dual–responsive release was tested by combining GSH with pH conditions, as shown in Fig. 4. When GSH was used at 10 mM (Fig. 4B), it was observed that the SA cumulative release increased in this order: pH 5.5 > 6.8 > 7.4. In this connection, KC–SA1 released a higher SA than KC–SA2 and reached ~ 48% (pH 5.5), ~ 31% (pH 6.8), and 18% (pH 7.4). This result demonstrates the positive impact toward high release due to GSH addition. From this point, we further increased the GSH concentration to 20 mM to ensure that the release increased. As shown in Fig. 4C, as expected, the increment of GSH to 20 mM significantly increased SA release to ~ 98% (pH 5.5), ~ 69% (pH 6.8), and ~ 46% (pH 7.4), as indicated from KC–SA1. This confirms that as the amount of GSH increases in the release medium, the release increases as the solubility also increases, i.e., the medium becomes more favorable for the release of SA. All release patterns could be described by two stages of zero-order release (up to 7 h) and sustained from 7 h to 15 days. From the literature survey, most fabricated delivery systems for EOs demonstrate two-stage release, but the first stage is the burst release effect followed by the sustained stage. For instance, the release of *Carum copticum* EO from chitosan nanoparticles exhibits an initial burst release within 20 h, then a sustained release within 100 h, and a higher release is observed under acidic pH conditions (Esmaeili and Asgari 2015). Similarly, peppermint and green tea EOs display a two-stage pattern of burst and sustained effects, varying under pH conditions, and the release kinetics follow the Fickian model (Shetta et al. 2019). Concerning the release of EOs from MSNs, SBA-15 represents a sustained long-term release of the thymol component of ~ 27% in the first 24 h and continued for 31 days (release of approximately 69%) (Gámez et al. 2020). In another study, (Cadena et al. 2018) demonstrated that the cinnamaldehyde component releases approximately 50% from lactose capping–MSNs after 24 h, and no release for cinnamaldehyde was observed after 48 h.

To determine the release kinetics, the obtained release profiles were fitted to various kinetic models (i.e., zero-order, first-order, Hixson–Crowell, Korsmeyer–Peppas, and Higuchi). Fitting data to linear regression modeling indicated that SA was released during the first 6 h according to zero-order kinetics ($R^2 = 0.98$–1.00). Alternatively, fitting data to both linear and nonlinear regressions revealed that the SA release under all conditions for 15 days best fit the Korsmeyer–Peppas model (Additional file 1: Tables S2–S4). The drug release based on this model is proposed to degrade or erode nanoformulation material transporting the drug (Costa and Sousa Lobo 2001; Rothstein et al. 2009). MSNs, as drug carriers, are porous materials, so degradation is largely restricted only to the outermost layer and does not affect the interior surface of MSNs (Pham et al. 2020). Tables show the release kinetics parameters of release efficiency (RE, %) and mean release time (MRT, h). The RE of SA from nanoformulations significantly increased as pH decreased to 5.5 (low acidity) and GSH increased to 20 mM (higher concentration), as shown in Additional file 1: Table S4. Consequently, this could be proper for efficient SA release from MSNs. MRT is ascribed as the mean time required to achieve the maximum release for a drug or pharmaceutical agent from its carrier or dosage form. The results demonstrate that the MRT of SA significantly decreases when the nanoformulations were exposed to low acidic pH combined with high GSH concentration. This reflects the efficiency of the intended nanoformulations that permit easier SA release from MSNs into the surrounding medium because of the increased

solubility, as supported by the solubility data. Screening the literature indicates that various kinetic models have been reported for EOs from many carriers. de Oliveira, Paula, and Paula 2014 demonstrated that *Lippiasidoides* EO is released from alginate/cashew gum nanoparticles through the Korsmeyer-Peppas kinetics model. Additionally, jasmine EO release from pectin/chitosan nanoparticles follows the Korsmeyer-Peppas kinetics model (Attallah et al. 2020). Apart from this model, the release kinetics of sucupira EO loaded in nanostructured lipid carriers fit the first-order kinetics (Vieira et al. 2020), cinnamon EO releases from spherical β-cyclodextrin/chitosan nanoparticles according to Fickian diffusion (Matshetshe et al. 2018), and the myrcene component encapsulated in the cyclodextrin matrices (CD, β-CD, γ-CD, and 2-hydroxypropyl-β- (HP-β-CD) follows the diffusion mode. (Li et al. 2020).

Overall, the release kinetics results showed that the least efficient release medium was PBS 7.4, which would be highly adventitious, as it assures the integrity of the whole drug content within MSNs as they circulate along the bloodstream until they reach their targeted cancer cells. The kinetic order by which the EO is released is mainly the Korsmeyer-Peppas order along the 15-day release interval, which is typical for such a porous nanoparticulate carrier system. However, the release of SA during the first 6 h followed zero-order kinetics would be considered adventitious, as the release of EO along that time would not be affected by its concentration. This is an important trait for EO release, as it is very slow during the early release period. Pores on the MSN surface are suggested to be the ones responsible for maintaining the release behavior within the zero-order kinetic model boundary for the short period, and then governing SA from the nanoparticle structure is typical for maintaining the release of SA on a Korsmeyer-Peppas kinetic model basis. As the efficiency of nanoformulations is considered, KC–SA1 (with high drug content) generally showed a significantly higher mean cumulative percent of SA released, as well as better RE, than KC–SA2. The highest significant system efficiency was observed when using PBS at low acidic pH combined with 20 mM GSH, compared to the release of either KC–SA1 or KC–SA2 in comparative media. The release behavior for SA from both nanoformulations can be simply described as sustained, with the highest mean cumulative percent due to a dual–trigger release effect by pH and GSH for a long time over 15 days. Intriguingly, these results provide insights into the expected pharmacological behavior either in targeted tumor drug delivery systems for various cancer cells or in vivo.

Cytotoxicity and anticancer evaluation

Figure 5 shows that cell viability was significantly ($p < 0.05$) dependent on the cell line and concentration of KC. The cell viability was ranked in the order MRC5 (employed as normal cells) > HepG2 > HL60 after 48 h of treatment. Cell viability reached approximately 60%, 39%, and 39% for MRC5, HepG2, and HL60 cells, respectively, when cells were treated at 1000 μg/ml. As expected, the higher concentration of KCC significantly inhibited cell viability for all tested normal and cell lines. KCC had an increased inhibitory effect on the investigated cancer cells compared with normal cells. This observation displays moderate biocompatibility toward MRC5 cells but was toxic for HepG2 and HL60 cells, especially when cells were treated with 1000 μg/ml.
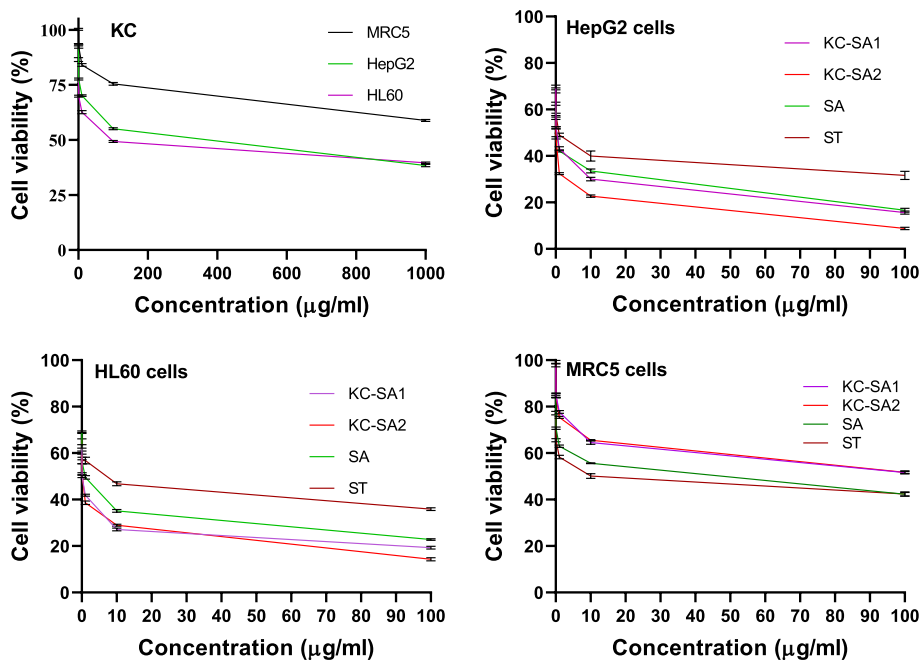
Fig. 5 Cytotoxicity evaluation of KC nanoparticles and nanoformulations on MRC5 normal cells and HepG2 liver and HL60 leukemia cancer cells treated with different concentrations and incubated for 48 h

Table 4 The IC50 values were obtained for normal and cancer cells

Formula	IC50 µg/ml		
	MRC5	HepG2	HL60
KC	1689 ± 47	186.15 ± 9.2	102.9 ± 7.31
KC-SA1	174.6 ± 5.8	0.24 ± 0.02	0.13 ± 0.01
KC-SA2	120 ± 4.33	0.038 ± 0.004	0.08 ± 0.01
SA	14.9 ± 1.29	0.14 ± 0.01	0.4 ± 0.06
STS	25.74 ± 1.28	5.53 ± 0.19	14.96 ± 0.83

The anticancer effects using the MTT assay indicated that the nanoformulations SA and STS significantly affected cell viability depending on the concentration and cell line. In this context, obtaining high cell viability indicates fewer cytotoxic effects/anticancer effects, but obtaining low cell viability values indicates a high cytotoxic effect/anticancer effect. Interestingly, HL60 cell viability was decreased compared to MRC5 and HepG2 cells. Additionally, at high concentrations, cell viability was highly inhibited compared to that at lower concentrations. In the case of HepG2 cells, the anticancer activity was detected in the following order: KC-SA2 > KC-SA1 > SA > STS. At a concentration of 100 µg/ml, KC-SA2 inhibited HepG2 cell viability to ∼8%, compared to ∼15%, ∼16%, and ∼31% with KC-SA1, SA, and STS, respectively. In the case of HL60 cancer cells, the anticancer effects were ranked as follows: KC-SA2 > KC-SA1 > SA > STS. Treating HL60 cells at 100 µg/mL significantly constrained cell viability to ∼18%, ∼14%, ∼22%, and ∼35% with KC-SA1, KC-SA2, SA, and STS, respectively. In the case of MRC5 normal cells, the cytotoxicity was recorded in the following order: ST > SA > KC-SA1 > KC-SA2.

The treatment of cells at 100 µg/mL highly decreased the MRC5 viability to ~ 51% and ~ 40%, respectively, for nanoformulations and SA or STS. From the obtained results, the nanoformulations are likely rather than SA or STS due to their lower toxic effects on MRC5 cells.

The obtained results were subjected to IC50 calculations; thus far, the IC50 calculation (Table 4) provides a comparison between all treatments and cells. For MRC5 normal cells, SA had a lower IC50 value (~ 15 µg/ml) than ST (~ 26 µg/mL), KC-SA2 (~ 120 µg/mL), KC-SA1 (~ 175 µg/mL), and KC (~ 1690 µg/mL). These results indicate that KC seems biocompatible for MRC5 normal cells, but SA shows high toxicity compared to nanoformulations, which display moderate toxicity. For HepG2 and HL 60 cancer cells, the nanoformulations were more effective than SA, STS, or KC. The anticancer pattern was ranked in HepG2 cells as KC-SA2 (~ 0.04 µg/mL) > SA > KC-SA1 > ST > KC, whereas in HL60 cells, it was ranked as KC-SA2 (~ 0.08) > KC-SA1 > SA > STS > KC. Due to the anticancer effects on HepG2 and HL60 cells having closed each other, HL60 cells were more sensitive to KC than HepG2 cells; consequently, we continued further studies on HL60 cells along with the urgent need to search for effective therapy for leukemia cancers.

Molecular targeting and anticancer mechanisms

Caspase-3 activation in HL60 leukemia cancer cells   In most cancer cells, the apoptotic cell death route occurs by the caspase pathway because it can cleave and inactivate many cellular proteins (McIlwain, Berger, and Mak 2013). As indicated by the caspase-3 results in Fig. 6A, no significant difference was noticed between HL60 cells and KCs. Therefore, KC does not affect caspase-3 activity, thus acting only as a drug nanocarrier. Nanoformulations and SA significantly ($p < 0.05$) enhanced caspase-3 activity compared to HL60 control cells, SA, and KC. Importantly, the nanoformulations showed a higher caspase-3 than SA in HL60 cells. We observed that caspase-3 was improved in this order: KC-SA2 > KC-SA1 > SA, showing the importance of nanoformulations compared to SA. The obtained results are in good agreement with our previously published data for thymoquinone and colchicine natural agents (AbouAitah et al. 2018, 2020a).

Induction of intracellular cytochrome c release

We determined the intracellular release of cytochrome c because it is an indicator of the inhibition of cancer cells via an apoptosis pathway. As expected, cytochrome c release significantly accumulated when cells were treated with nanoformulations, free SA and STS compared to untreated HL60 cells and KCs (Fig. 6B). Nevertheless, no significant differences were noticed among the four treatments. KC–SA2 had a slightly increased cytochrome c release in HL60 cells compared with the others. The results are in line with our previous data showing that nanoformulations composed of thymoquinone (an essential oil component) improved cytochrome c release in brain cancer cells (Shahein et al. 2019). These results suggest that the enhanced intracellular cytochrome c promotes the activation of apoptotic cell death, and these results are linked to caspase–3 induction; both are highly indicative of apoptosis.
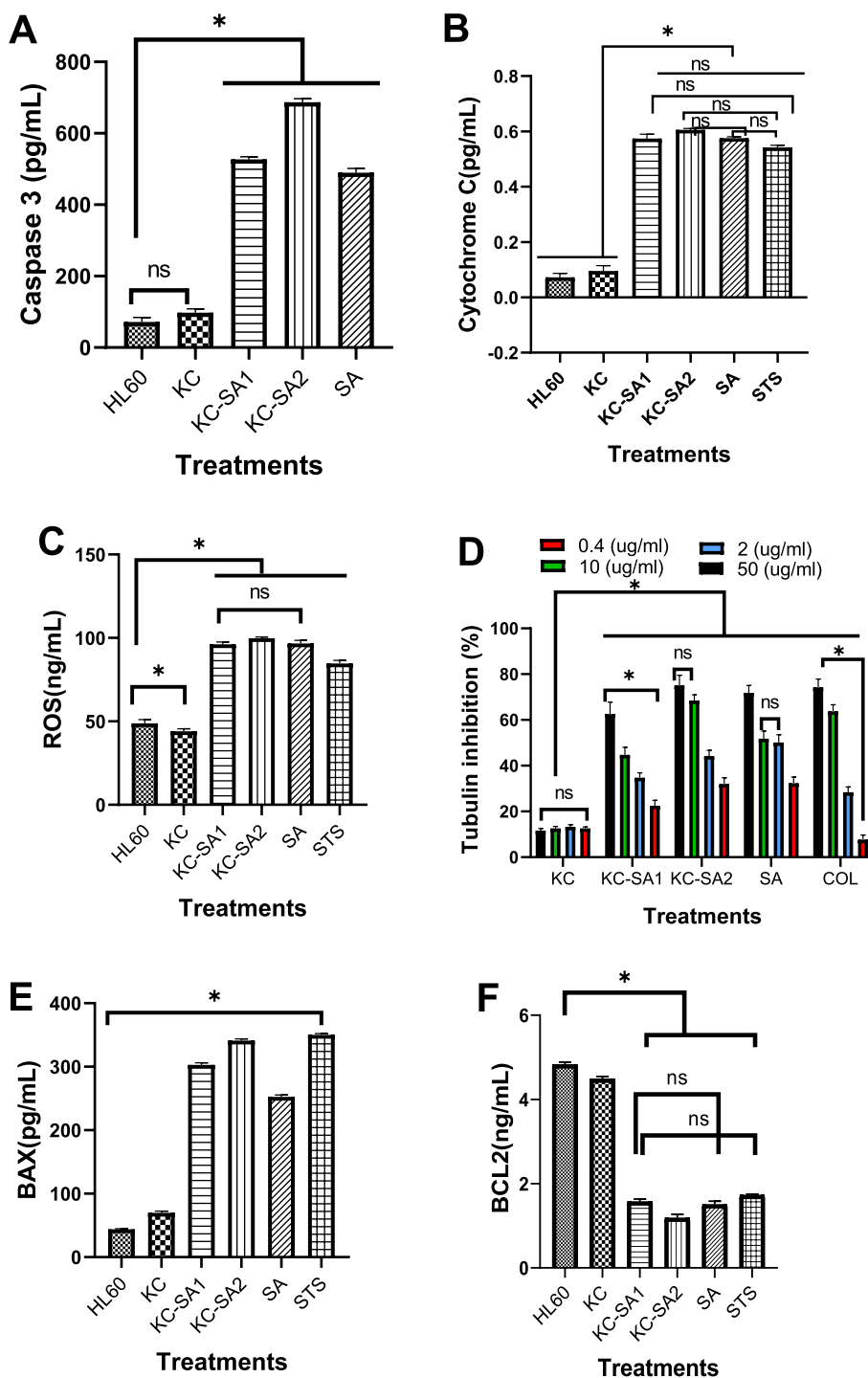
Fig. 6 The possible molecular targets in HL60 leukemia cancer cells treated with different materials after 48 h

Generation of ROS

Reactive oxygen species (ROS) consist of highly reactive molecules (free radicals: hydroxyl (HO*) and superoxide (O2*) and nonradical molecules, i.e., hydrogen peroxide (H_2O_2)), regulating several signaling pathways in cancers. (Perillo et al. 2020)

reviewed that the negative or positive impacts of ROS are strongly dependent on their expression level in cancer cells. It is accepted that ROS at moderate levels is needed to induce several cellular functions, i.e., gene expression, and increased ROS expression in tumor cells is related to an increased metabolic rate and gene mutation. However, with more increases, ROS can produce several pathologic conditions, including tumor promotion and progression, due to their versatile signaling pathways. However, it is also acceptable that ROS contribute to triggering apoptosis in cancers. Therefore, ROS have double-faced actions in cancers. There is evidence for increasing ROS in AML cancer (Sillar et al. 2019; Robinson et al. 2020). Therefore, we tested whether the nanoformulations were able to modulate ROS in HL60 cells. Figure 6B shows a significant difference when the cells were exposed to all treatments. KC reduced ROS levels compared with control cells, while nanoformulations, SA, and STS significantly promoted ROS levels in treated cells compared with control cells. No significant differences were observed for nanoformulations, and SA compared to STS increased ROS levels from ~50 ng/mL to ~100 ng/mL. These results are in agreement with data by (El Khoury et al. 2020) on AML cells, where natural extract promotes ROS, activating apoptosis. A nanoformulation tailored by celastrol-loaded nanoparticles amplifies intracellular ROS, consequently promoting apoptosis in ovarian cancer (Niu et al. 2020). Targeting ROS via either induction or inhibition provides a novel therapeutic for AML cancer (Sillar et al. 2019); accordingly, our results seem promising.

Inhibition of tubulin activity

Screening drugs or active agents for their tubulin inhibition and gaining antimitotic drugs are urgently required in cancer therapy. Antimitotic drugs are mostly toxic agents that induce a specific killing of cancer cells because they affect cell divisions, as they are characterized much faster than normal cells. A very good example of an efficient natural antimitotic agent is colchicine, but it is associated with considerable toxicity. Therefore, we examined whether the nanoformulations inhibited tubulin activity in HL60 cells. Figure 6 shows that inhibition of tubulin in HL60 cells was significantly related to concentrations. High tubulin inhibition was obtained when HL60 cells were treated with a high concentration gradually increasing to 50 μg/mL for all treatments. A significant difference ($p < 0.05$) was observed for nanoformulations, SA, and colchicine (COL) but not KC. It was found that the tubulin inhibition upon treating cells at 50 μg/mL was in the order KC–SA2 (~75%) > COL (~74%) > SA (~71%) > KC–SA1 (~62%). Notably, no significant differences were obtained when cells were treated with nanoformulations, especially KC–SA2 or colchicine, indicating the positive effect of using SA possessing a safe profile in contrast to colchicine antimitotic agents. The results agree with our previous study for colchicine-developed nanoformulation using MSNs.(AbouAitah et al. 2020a). We propose that the action by which nanoformulations or SA effectively inhibited tubulin is binding via colchicine binding sites, destabilizing tubulin and ultimately interfering with microtubule dynamics (Lu et al. 2012). This is because colchicine inhibited tubulin in HL60 to nearly a similar percent to nanoformulations or SA. The importance of tubulin inhibition is not only for arresting the cell cycle at the G2/M phase (Blajeski et al. 2002) but also for allowing apoptotic cell death (Kulshrestha et al. 2017).

*Modulation of pro-apoptotic proteins (Bax/Bcl-2) in HL60 leukemia cells*

Cancer is a complex environment, and some proteins act as antiapoptotic proteins in many cancers, promoting cell survival and blocking apoptotic cell death. BCL-2 is an antiapoptotic agent that potent prevents cancer cells from death upon its upregulation (Vaux et al. 1988; Scherr et al. 2016). In contrast, Bax is a pro-apoptotic protein, indicating apoptosis; however, it is always found in many cancers in an activated condition. [63, 67]. Therefore, the modulation effect between both proteins is likely anticancer. Figure 6E and F shows that the nanoformulations SA and STS significantly inhibited BCL-2 compared to untreated HL60 cells. Maximum inhibition of BCL-2–1.18 ng/mL was observed for KC-SA2 compared to others. The inhibition of BCL-2 was found in the following order: KC-SA2 > SA > KC-SA1 > STS. Concerning BAX, treating cells with nanoformulations, free SA, and STS resulted in a significant-high increment of BAX compared to untreated HL60 cells. Activation of the BAX effect was observed and ranked as follows: STS > KC-SA2 > KC-SA1 > SA > KC. The nanoformulation, especially KC-SA2, activated BAX closely to the staurosporine drug; additionally, the use of nanoformulations highly increased BAX accumulation in cells compared with free SA. Taken together, the results of BCL2 and BAX indicate the potential modulation of BCL-2 (inhibition) and BAX (increment) and better molecular targeting in HL60 cells by nanoformulations. At the same time, this modulation generates apoptotic HL60 cells, as indicated by the caspase-3 activation results. Consequently, the results suggest the killing of HL60 cells due to apoptosis induction and interconnection with BCL-2 and BAX modulation (AbouAitah et al. 2020a).

Promotion of P21 protein

P21 is a tumor suppressor that arrests the cell cycle (at G1-S and G2-M phases) (Bunz et al. 1998; Harper et al. 1993) through modulation of p53 protein and cyclin-dependent kinase (CDK) inhibitors (Gartel and Tyner 1999). This is due to the interaction between cell cycle inhibition and apoptosis initiation, which is highly regulated by p53 protein functions, determining the response and sensitivity of tumors to drugs and inducing apoptosis, including leukemia (Wei et al. 2006; Davies et al. 2015). The accumulation of P21 in HL60 cells was measured, and the related results are depicted in Fig. 7A. The upregulation of p21 in treated cells compared to control cells that received KC was demonstrated. The efficiency of treatments for P21 promotion followed the order KC–SA2 > KC–SA1 > SA > STS. Furthermore, KC–SA2 significantly increased nearly 13–fold change and 13–fold change, respectively, when compared to the control cell (~ onefold change). Thus, the nanoformulations could be novel nano-delivery agents modulating the p21 protein in AML cancer.

Expression of PARP1

Poly(ADP-ribose) polymerase (PARP) is a promising target in cancers. It is known as a DNA repair protein because it has a key function specifically in nucleotide or base excision repair of DNA damage, which includes the DNA breaks initiated due to the use of drugs (Morales et al. 2014). Because there are several forms of PARP, PARP1 enhances DNA repair (Gibson and Kraus 2012). In many cancers, including AML, there is evidence that PARP1 is upregulated. (Ossovskaya et al. 2010; Li et al. 2019) Therefore, we
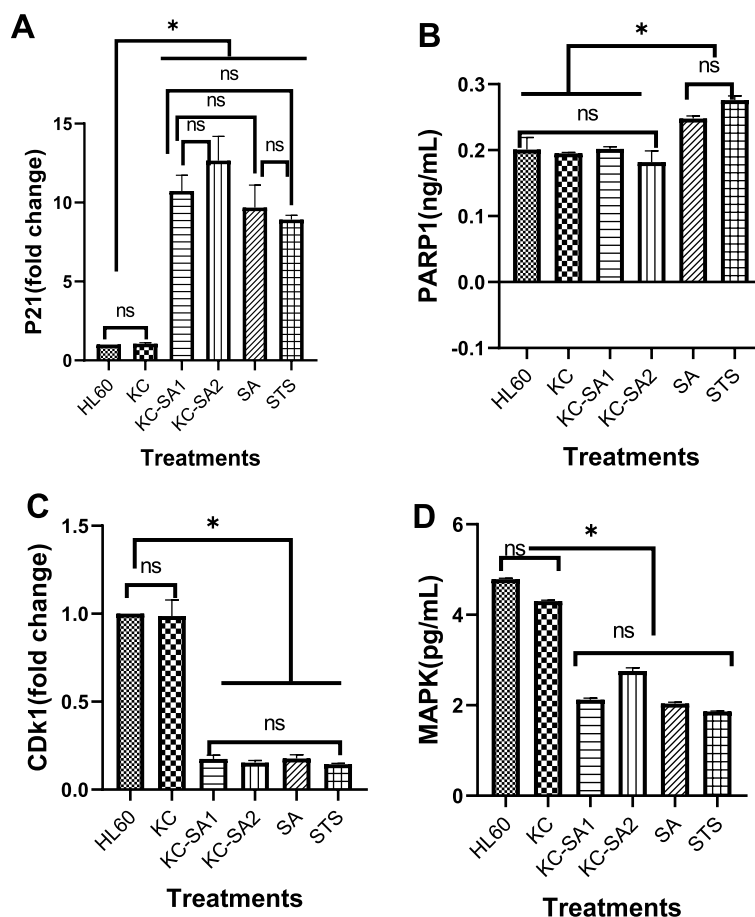
Fig. 7 The possible molecular targets in HL60 leukemia cancer cells treated with different materials after 48 h

determined PARP1 levels, and the results are indicated in Fig. 7B. No significant differences between control cells and KC, KC–SA1, and KC–SA2 were obtained. Of note, treating cells with SA and STS significantly elevated PARP1 levels.

Inhibition of CDK1

Including leukemia cancers, cyclin-dependent kinases (CDKs) play important roles in regulating cancer initiation, the cell cycle, transcription, apoptosis, proliferation, and DNA repair (Richter et al. 2021). Since the FDA has approved some CDK inhibitors for cancers (e.g., palbociclib, ribociclib, and abemaciclib), representing promising molecular targets in leukemia cancers (Lee and Zeidner 2019). To verify the modulation of CDK1, we analyzed CDK1, and the results are shown in Fig. 7C. No significant difference in CDK1 expression was detected by exposing cells to KC. Alternatively, a significant difference in CDK1 accumulation was observed when cells received nanoformulations, SA, and STS; the inhibition was almost ~ 0.1–fold change compared to control cells with onefold change. Regardless of the treatments used by

nanoformulations or SA or STS, there was no significant difference between them. These observations indicate that KC had no effect on CDK1, and nanoformulations and SA exhibit similar efficiency as CDK1 inhibitors such as the STS reference drug. The efficiency of CDK1 inhibitors in AML cancer.

Inhibition of MAPK

To further identify the possible inhibition of MAPK in HL60 cells, we assessed the level of MAPK, and the results are presented in Fig. 7D. MAPK expression decreased upon treating cells with nanoformulations, SA, and STS in comparison to control cells and KCs. The efficiency for constraining MAPK was detected in the order STS > SA > KC–SA1 > KC–SA2; however, there were no significant differences among them. This observation demonstrates that either SA or nanoformulations effectively inhibit the MAPK pathway.

Targeting of long noncoding RNAs

LncRNAs are defined as noncoding transcripts that contain more than ~ 200 nucleotides in length (Kopp and Mendell 2018). The molecular targets for lncRNAs have revolutionized treatment for tumors, coming with recent accumulating evidence that lncRNAs potentially modulate many pathways in cancers, including AML, due to their regulatory role, e.g., cell cycle, apoptosis, cell proliferation, invasion, and metastasis, and may offer a novel approach and potential effectiveness for cancer treatments (Heo et al. 2019; Tsai et al. 2012; Shaker et al. 2017). Therefore, we evaluated whether nanoformulations target the LncRNAs HOTAIR, CCAT1, HULC, and H19.

Attenuation of HOTAIR

HOTAIR is a polyadenylated RNA that has 2158 nucleotides with 6 exons and is transcribed from the antisense strand of the HOXC gene cluster, specifically located between HoxC11 and HoxC12 on chromosome 12q13.13 (Woo and Kingston 2007). Several studies have demonstrated that HOTAIR is involved in many pathways (i.e., tumorigenesis, invasion, growth, cell differentiation, metastasis, and drug resistance in cancers) (Tang and Hann 2018). Consequently, HOTAIR has emerging potential for diagnosis and novel therapeutic targets, including AML, since it is upregulated (Hao and Shao 2015). We found that all treatments significantly attenuated HOTAIR in treated HL60 cells compared to untreated cells (~ 15-fold change). Inhibition of HOTAIR was detected in low–fold change in this order SA (~ 1.2– fold change) > KC–SA2 (~ 2.6–fold change) > KC–SA1 (~ fivefold change) > KC (~ 7.7–fold change) > STS (~ 8.1–fold change) (Fig. 8A). The observation that KC inhibited HOTAIR (unexpected) consequently provides evidence that the construction of nanoformulations with KC is promising. The obtained data demonstrate that knockdown of HOTAIR may induce apoptosis in HL60 cells because silencing HOTAIR decreases cell growth, induces apoptosis, and reduces colony formation in AML cells (Tang and Hann 2018).
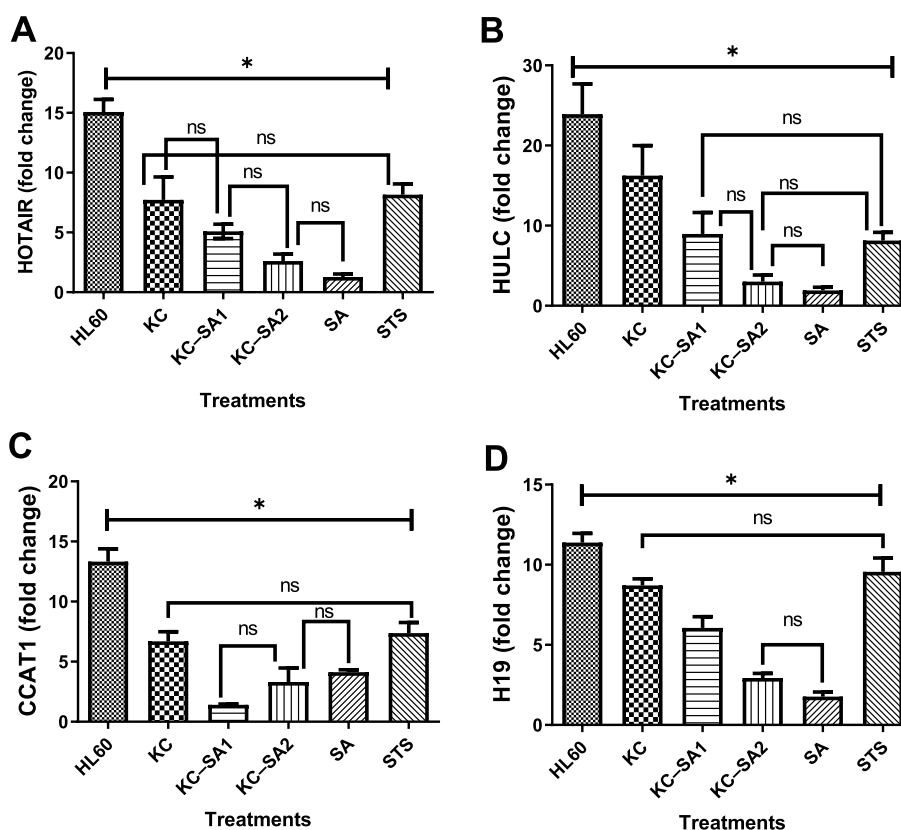
Fig. 8 The possible long noncoding RNAs targets in HL60 leukemia cancer cells treated with different materials after 48 h

Attenuation of HULC

HULC is located on chromosome 6p24.3 and is conserved in primates (Panzitt et al. 2007), and its transcription is approximately 500 nucleotides long, spliced, polyadenylated, and localized in the cytoplasm (Wang et al. 2010). In a study by (Lu et al. 2017), they showed that HULC is remarkably overexpressed in chronic myeloid leukemia, and they also demonstrated that knockdown of HULC significantly induces apoptosis by repressing Bcl–2 expression. As indicated by Fig. 8B, all treatments significantly inhibited HULC in treated cells compared with control cells; however, the inhibition varied. A higher reduction of HULC expression was detected for cells exposed to SA (~ twofold change) and KC–SA2 (~ threefold change) compared to control cells (~ 24–fold change). This suggests that SA as a free source or in nanoformulation is an effective natural substance that may be considered a new target for HULC with further exploration. We believe that repressing HULC is associated with the inhibition of Bcl–2, as indicated in Fig. 6, considerably leading to triggered apoptosis in HL60 cells.

Knockdown of CCAT1

Colon cancer-associated transcript 1 (CCAT1) lncRNA, which was first isolated from colon cancer and is 2628 nucleotides long and presented on chromosome 8q24.2, has received much attention due to its high expression pattern accompanied by an onco-genic role in many cancers, including AML (Liu, Chen, and Hann 2019; Chen et al. 2016). Its functions in cancers include tumor genesis, cancer progression, metastasis, patient survival, and the regulation of many target genes. Thus far, CCAT lncRNA could be severe for cancer diagnosis and therapy. The results showed that all treatments significantly reduced CCAT compared to the control. The most effective treatment was KC–SA1 (Fig. 8C). (Chen et al. 2016) demonstrated that CCAT1 represses monocytic differentiation and promotes HL–60 cell growth by downregulating the tumor-suppressive miR-155. This could provide a new therapeutic way to target CCAT1 for cancer treatments.

Inhibition of H19

The endogenous H19 gene is located on chromosome 11p15 and plays an important role in cancer initiation and progression. (Raveh et al. 2015) Many studies have iden-tified that depending on the cancer type, H19 may act as an oncogene or tumor sup-pressor (Li et al. 2014a, b; Raveh et al. 2015). Accumulating evidence suggests that H19 is upregulated (Zhang et al. 2018; Zhao and Liu 2019) in AML. The treatment of HL60 cells with all treatments significantly inhibited H19 rather than control cells. Additionally, lower H19 expression was observed in cells treated with SA and KC–SA2 (Fig. 8D).

Inhibition of matrix metalloproteinases (MMPs)

The family of matrix metalloproteinases (MMPs) are zinc-dependent endopeptidases that are both intracellularly and membrane-bound. The members of the family cause deterioration of extracellular matrix (ECM) proteins (i.e., collagen, laminin, elastin, fibronectin); consequently, they affect various physiological and pathological processes, including cancers, by remodeling the ECM (Vu et al. 2018). In this connection, members
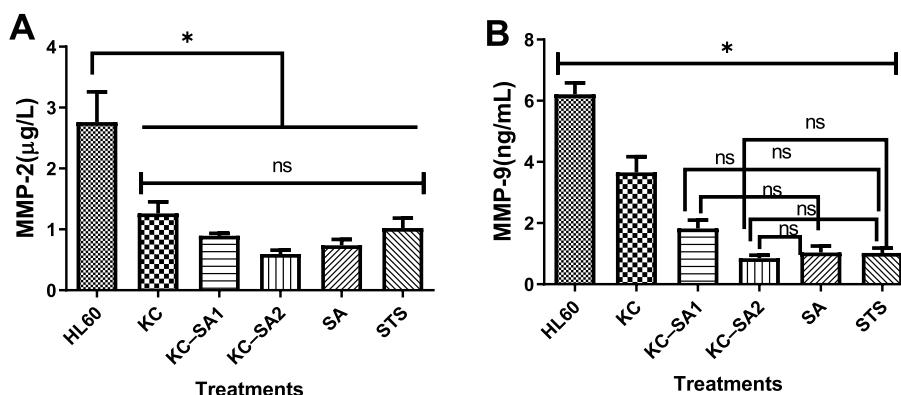
Fig. 9 The possible matrix metalloproteinases (MMPs) target in HL60 leukemia cancer cells treated with different materials after 48 h

Table 5 Summary of the possible targeting specifications in HL60 cancer cells by nanoformulations and free SA natural agent

Targeting specification	Treatments			Therapeutic efficacy *(As general effect)*
	Nanoformulations	SA	STS	
Caspase–3	Up	Up	Up	Nanoformulations > SA > STS
Cytochrome c	Up	Up	Up	Nanoformulations > SA > STS
ROS	Up	Up	Up	Nanoformulations > SA > STS
Tubulin inhibition	Up	Up	Up*	Nanoformulations > COL > SA
BAX	Up	Up	Up	STS > nanoformulations > SA
Bcl–2	Down	Down	Down	Nanoformulations > SA > STS
P21	Up	Up	Up	Nanoformulations > SA > STS
PARP1	Down (little)	Up (little)	Up (little)	Nanoformulations < SA < STS
CDK1	Down	Down	Down	Nanoformulations < STS < SA
MAPK	Down	Down	Down	STS < SA < nanoformulations
HOTAIR	Down	Down	Down	SA < nanoformulations < STS
HULC	Down	Down	Down	SA < nanoformulations < STS
CCAT1	Down	Down	Down	Nanoformulations < SA < STS
H19	Down	Down	Down	SA < nanoformulations < STS
MMP–2	Down	Down	Down	nanoformulations < SA < STS
MMP–9	Down	Down	Down	Nanoformulations < SA < STS

*The standard drug used was colchicine as a tubulin inhibitor. Up and down refer to the expression or level of tested markers. Up means that the treatment promotes the regulation of the tested marker, and down means that the treatments inhibit the regulation of the maker

of the family, especially MMP–2 and MMP–9, are known for their remarkable role in tumor growth and metastasis, as they can degrade collagen IV in the ECM (Klein et al. 2004). Furthermore, both MMP–2 and MMP–9 are often upregulated in cancer cells, including ALL and AML, with valuable prognostic impact (Vu et al. 2018; Klein et al. 2004; Kossakowska et al. 1999; Lin et al. 2002; Suminoe et al. 2007). Recently, screening new inhibitors and developing a new strategy for MMP drug delivery have brought new insights into tumor targeting (Cathcart et al. 2015; Ling-Li et al. 2020). From this considerable point, we thus tested the possibility of nanoformulations targeting MMP–2 and MMP–9 in HL60 cells.

Inhibition of MMP–2 and MMP–9

Figure 9 displays the significant reduction in both MMP–2 and MMP–9 in HL60 cells treated with KC, nanoformulations, SA, and STS compared to the control. Generally, KC–SA2 had a higher reduction in MMP–2 and MMP–9, followed by SA, STS, and KC–SA1. However, there was almost no significant difference between them. Furthermore, KC was considerably decreased the expression, especially MMP–2, compared with MMP–9. This result demonstrates the possible contribution of the MSN nanocarrier together with SA. The obtained data suggest that nanoformulations and SA act as MMP inhibitors. Additionally, our findings show that natural agents such as EOs offer a new target for targeting leukemia cancer as indicated on HL60 cells, creating an opportunity to further develop a novel strategy to target MMPs with natural substances. Table 5 summarizes the possible mechanism of action obtained from our results.

Conclusions

We successively developed new nanoformulations for SA as a model of EOs constructed by MSNs. The nanoformulations had SA contents up to ~52%, enabling sustained SA release under dual-responsive triggers by pH (low) and GSH (high concentration), similar to the tumor environment, ideally for cancer targeting. The results demonstrated that SA was typically governed by nanoformulations on the Korsmeyer-Peppas kinetic model basis. From the cytotoxicity evacuations, MSNs exhibited moderate biocompatibility with MRC5 normal cells but were toxic to HepG2 and HL60 cancer cells specifically at high concentrations (1000 µg/mL). Generally, the nanoformulations enhanced the anticancer effects against both HepG2 liver cells and HL60 leukemia cells compared to SA. The mechanism of action and molecular target studies on HL60 cells demonstrated that most of the nanoformulations had positive modulatory effects on many signaling pathways involved in the apoptosis cell death pathway and genetic regulation. We found a remarkable promotion in caspase–3, cytochrome c, ROS, tubulin inhibition, BAX, and P21 expression; on the other hand, we found a considerable inhibition in PARP1, CDK1, and MAPK expression. Most importantly, new results were obtained on the genetic regulation principle. The results showed that nanoformulations or SA (in some cases) highly inhibited lncRNAs (HOTAIR, HULC, CCAT1, and H19) and matrix metalloproteinases (MMP–2 and MMP–9) and may provide a novel leukemia target.

Therefore, the developed nanoformulations with SA as a model EO have promising applications in drug delivery for targeting cancers and could serve as new antileukemia agents with further deep preclinical studies.

Supplementary Information

The online version contains supplementary material available at https://doi.org/10.1186/s12645-022-00152-9.

> **Additional file 1: Table S1.** The solubility properties of SA oil under different media. **Table S2.** In vitro release kinetics of nanoformulations in PBS of different pH values. **Table S3.** In vitro release kinetics of nanoformulations in 10mM GSH/PBS of different pH values along 15 days. **Table S4.** In vitro release of nanoformulations in 20mM GSH/PBS of different pH values along 15 days.

Availability of data and materials
All data presented in the work.

Declarations

Ethics approval and consent to participate
All studies were performed based on in vitro assays.

Consent for publication
Not applicable.

Competing interests
The authors declare that they have no competing interests.

References

AbouAitah KEA, Farghali AA, Swiderska-Sroda A, Lojkowski W, Razin AM (2016) Mesoporous silica materials in drug delivery system: pH/glutathione-responsive release of poorly water-soluble pro-drug quercetin from two and three-dimensional pore-structure nanoparticles. J Nanomed Nanotechnol 7(2):1–12

AbouAitah K, Swiderska-Sroda A, Farghali AA, Wojnarowicz J, Stefanek A, Gierlotka S, Opalinska A, Allayeh AK, Ciach T, Lojkowski W (2018) Folic acid-conjugated mesoporous silica particles as nanocarriers of natural prodrugs for cancer targeting and antioxidant action. Oncotarget 9(41):26466–26490. https://doi.org/10.18632/oncotarget.25470

AbouAitah K, Hassan HA, Swiderska-Sroda A, Gohar L, Shaker OG, Wojnarowicz J, Opalinska A, Smalc-Koziorowska J, Gierlotka S, Lojkowski W (2020a) Targeted nano-drug delivery of colchicine against colon cancer cells by means of mesoporous silica nanoparticles. Cancers 12(1):144. https://doi.org/10.3390/cancers12010144

AbouAitah K, Stefanek A, Higazy IM, Janczewska M, Swiderska-Sroda A, Chodara A, Wojnarowicz J, Szałaj U, Shahein SA, Aboul-Enein AM, Abou-Elella F, Gierlotka S, Ciach T, Lojkowski W (2020b) Effective targeting of colon cancer cells with piperine natural anticancer prodrug using functionalized clusters of hydroxyapatite nanoparticles. Pharmaceutics 12(1):70

AbouAitah K, Higazy IM, Swiderska-Sroda A, Abdelhameed RM, Gierlotka S, Mohamed TA, Szałaj U, Lojkowski W (2021) Anti-inflammatory and antioxidant effects of nanoformulations composed of metal-organic frameworks delivering rutin and/or piperine natural agents. Drug Deliv 28(1):1478–1495. https://doi.org/10.1080/10717544.2021.1949073

Ahmadi S, Fazilati M, Nazem H, Mousavi SM (2021) Green synthesis of magnetic nanoparticles using *satureja hortensis* essential oil toward superior antibacterial/fungal and anticancer performance. Biomed Res Int 2021:8822645. https://doi.org/10.1155/2021/8822645

Aljuffali IA, Fang CL, Chen CH, Fang JY (2016) Nanomedicine as a strategy for natural compound delivery to prevent and treat cancers. Curr Pharm Des 22(27):4219–4231. https://doi.org/10.2174/1381612822666160620072539

Ammar H, Ghorab MM, Mahmoud AA, Higazy IM (2013) Preformulation studies intended for targeted lamotrigine polymeric nanosuspension. Future 1:1

Ashley CE, Carnes EC, Phillips GK, Padilla D, Durfee PN, Brown PA (2011) The targeted delivery of multicomponent cargos to cancer cells by nanoporous particle-supported lipid bilayers. Nat Mater. https://doi.org/10.1038/nmat2992

Attallah OA, Shetta A, Elshishiny F, Mamdouh W (2020) Essential oil loaded pectin/chitosan nanoparticles preparation and optimization via Box-Behnken design against MCF-7 breast cancer cell lines. RSC Adv 10(15):8703–8708. https://doi.org/10.1039/C9RA10204C

Bansal A, Celeste Simon M (2018) Glutathione metabolism in cancer progression and treatment resistance. J Cell Biol 217(7):2291–2298. https://doi.org/10.1083/jcb.201804161

Blajeski AL, Phan VA, Kottke TJ, Kaufmann SH (2002) G(1) and G(2) cell-cycle arrest following microtubule depolymerization in human breast cancer cells. J Clin Invest 110(1):91–99. https://doi.org/10.1172/jci13275

Bouhtit F, Najar M, Agha DM, Melki R, Najimi M, Sadki K, Boukhatem N, Bron D, Meuleman N, Hamal A, Lagneaux L, Lewalle P, Merimi M (2021) New anti-leukemic effect of carvacrol and thymol combination through synergistic induction of different cell death pathways. Molecules (basel, Switzerland) 26(2):410. https://doi.org/10.3390/molecules26020410

Bunz F, Dutriaux A, Lengauer C, Waldman T, Zhou S, Brown JP, Sedivy JM, Kinzler KW, Vogelstein B (1998) Requirement for p53 and p21 to sustain G2 arrest after DNA damage. Science 282(5393):1497–1501. https://doi.org/10.1126/science.282.5393.1497

Cadena B, Marimar GM, Preston RAL, der Hoorn V, Townley HE, Thompson IP (2018) Species-specific antimicrobial activity of essential oils and enhancement by encapsulation in mesoporous silica nanoparticles. Ind Crops Prod 122:582–590. https://doi.org/10.1016/j.indcrop.2018.05.081

Cathcart J, Pulkoski-Gross A, Cao J (2015) Targeting matrix metalloproteinases in cancer: bringing new life to old ideas. Genes Dis 2(1):26–34. https://doi.org/10.1016/j.gendis.2014.12.002

Chen L, Wang W, Cao L, Li Z, Wang X (2016) Long non-coding RNA CCAT1 acts as a competing endogenous RNA to regulate cell growth and differentiation in acute myeloid leukemia. Mol Cells 39(4):330–336. https://doi.org/10.14348/molcells.2016.2308

Costa P, Lobo JMS (2001) Modeling and comparison of dissolution profiles. Eur J Pharm Sci 13(2):123–133. https://doi.org/10.1016/S0928-0987(01)00095-1

Davies C, Hogarth LA, Mackenzie KL, Hall AG, Lock RB (2015) p21(WAF1) modulates drug-induced apoptosis and cell cycle arrest in B-cell precursor acute lymphoblastic leukemia. Cell Cycle 14(22):3602–3612. https://doi.org/10.1080/15384101.2015.1100774

de Matos SP, Teixeira HF, de Lima ÁAN, Veiga-Junior VF, Koester LS (2019) Essential oils and isolated terpenes in nanosystems designed for topical administration: a review. Biomolecules 9(4):138. https://doi.org/10.3390/biom9040138

de Oliveira EF, Paula HCB, de Paula RCM (2014) Alginate/cashew gum nanoparticles for essential oil encapsulation. Colloids Surf B Biointerfaces 113:146–151. https://doi.org/10.1016/j.colsurfb.2013.08.038

Doherty GJ, McMahon HT (2009) Mechanisms of endocytosis. Annu Rev Biochem 78(1):857–902. https://doi.org/10.1146/annurev.biochem.78.081307.110540

Duan W, Du L, Jiang X, Wang R, Yan S, Xie Y, Yan K, Wang Q, Wang L, Zhang X, Pan H, Yang Y, Wang C (2016) Identification of a serum circulating lncRNA panel for the diagnosis and recurrence prediction of bladder cancer. Oncotarget 7(48):78850–78858. https://doi.org/10.18632/oncotarget.12880

El Khoury M, Haykal T, Hodroj MH, Najem SA, Sarkis R, Taleb RI, Rizk S (2020) Malva pseudolavatera leaf extract promotes ROS induction leading to apoptosis in acute myeloid leukemia cells in vitro. Cancers. https://doi.org/10.3390/cancers12020435

El-Leithy AS, El-Hanafy SH, Khattab ME, Ahmed SS, Ghafour A (2017) Effect of nitrogen fertilization rates, plant spacing and their interaction on essential oil percentage and total flavonoid content of summer savory (*Satureja hortensis* L.) plant. Egypt J Chem 60(5):805–816. https://doi.org/10.21608/ejchem.2017.1296.1074

Esmaeili A, Asgari A (2015) In vitro release and biological activities of Carum copticum essential oil (CEO) loaded chitosan nanoparticles. Int J Biol Macromol 81:283–290. https://doi.org/10.1016/j.ijbiomac.2015.08.010

Estey EH (2018) Acute myeloid leukemia: 2019 update on risk-stratification and management. Am J Hematol 93(10):1267–1291. https://doi.org/10.1002/ajh.25214

Farge T, Saland E, de Toni F, Aroua N, Hosseini M, Perry R, Bosc C, Sugita M, Stuani L, Fraisse M, Scotland S, Larrue C, Boutzen H, Féliu V, Nicolau-Travers ML, Cassant-Sourdy S, Broin N, David M, Serhan N, Sarry A, Tavitian S, Kaoma T, Vallar L, Iacovoni J, Linares LK, Montersino C, Castellano R, Griessinger E, Collette Y, Duchamp O, Barreira Y, Hirsch P, Palama T, Gales L, Delhommeau F, Garmy-Susini BH, Portais JC, Vergez F, Selak M, Danet-Desnoyers G, Carroll M, Récher C, Sarry JE (2017) Chemotherapy-resistant human acute myeloid leukemia cells are not enriched for leukemic stem cells but require oxidative metabolism. Cancer Discov 7(7):716–735. https://doi.org/10.1158/2159-8290.cd-16-0441

Feng L, Dong Z, Tao D, Zhang Y, Liu Z (2018) The acidic tumor microenvironment: a target for smart cancer nano-theranostics. Natl Sci Rev 5(2):269–286. https://doi.org/10.1093/nsr/nwx062

Fonseca-Santos B, Chorilli M (2020) The uses of resveratrol for neurological diseases treatment and insights for nanotechnology based-drug delivery systems. Int J Pharm. https://doi.org/10.1016/j.ijpharm.2020.119832

Foroozandeh P, Aziz AA (2018) Insight into cellular uptake and intracellular trafficking of nanoparticles. Nanoscale Res Lett 13(1):339. https://doi.org/10.1186/s11671-018-2728-6

Frank LA, Onzi GR, Morawski AS, Pohlmann AR, Guterres SS, Contri RV (2020) Chitosan as a coating material for nanoparticles intended for biomedical applications. React Funct Polym 147:104459. https://doi.org/10.1016/j.reactfunctpolym.2019.104459

Froiio F, Ginot L, Paolino D, Lebaz N, Bentaher A, Fessi H, Elaissari A (2019) Essential oils-loaded polymer particles: preparation, characterization and antimicrobial property. Polymers. https://doi.org/10.3390/polym11061017

Gámez E, Elizondo-Castillo H, Tascon J, García-Salinas S, Navascues N, Mendoza G, Arruebo M, Irusta S (2020) Antibacterial effect of thymol loaded SBA-15 nanorods incorporated in PCL electrospun fibers. Nanomaterials (basel, Switzerland) 10(4):616. https://doi.org/10.3390/nano10040616

Gartel AL, Tyner AL (1999) Transcriptional regulation of the p21((WAF1/CIP1)) gene. Exp Cell Res 246(2):280–289. https://doi.org/10.1006/excr.1998.4319

Gibson BA, Lee Kraus W (2012) New insights into the molecular and cellular functions of poly(ADP-ribose) and PARPs. Nat Rev Mol Cell Biol 13(7):411–424. https://doi.org/10.1038/nrm3376

Guamán-Ortiz LM, Orellana MIR, Ratovitski EA (2017) Natural compounds as modulators of non-apoptotic cell death in cancer cells. Curr Genomics 18(2):132–155. https://doi.org/10.2174/1389202917666160803150639

Hao S, Shao Z (2015) HOTAIR is upregulated in acute myeloid leukemia and that indicates a poor prognosis. Int J Clin Exp Pathol 8(6):7223–7228

Harper JW, Adami GR, Wei N, Keyomarsi K, Elledge SJ (1993) The p21 Cdk-interacting protein Cip1 is a potent inhibitor of G1 cyclin-dependent kinases. Cell 75(4):805–816. https://doi.org/10.1016/0092-8674(93)90499-g

He C, Yiping Hu, Yin L, Tang C, Yin C (2010) Effects of particle size and surface charge on cellular uptake and biodistribution of polymeric nanoparticles. Biomaterials 31(13):3657–3666. https://doi.org/10.1016/j.biomaterials.2010.01.065

Heo MJ, Yun J, Kim SG (2019) Role of non-coding RNAs in liver disease progression to hepatocellular carcinoma. Arch Pharmacal Res 42(1):48–62. https://doi.org/10.1007/s12272-018-01104-x

Hosseini SM, Hosseini H, Mohammadifar MA, Mortazavian AM, Mohammadi A, Khosravi-Darani K, Shojaee-Aliabadi S, Dehghan S, Khaksar R (2013) Incorporation of essential oil in alginate microparticles by multiple emulsion/ionic gelation process. Int J Biol Macromol 62:582–588. https://doi.org/10.1016/j.ijbiomac.2013.09.054

Hsiao PC, Chang JH, Lee WJ, Ku CC, Tsai MY, Yang SF, Chien MH (2020) The Curcumin analogue, EF-24, triggers p38 MAPK-mediated apoptotic cell death via inducing PP2A-modulated ERK deactivation in human acute myeloid leukemia cells. Cancers (Basel). https://doi.org/10.3390/cancers12082163

Jermy B, Rabindran D, Almohazey WA, Alamoudi RM, Palanivel NA, Dafalla H, Almofleh AA, Alfareed TM, Ravinayagam V (2021) Synergistic action of curcumin and cisplatin on spinel ferrite/hierarchical MCM-41 nanocomposite against MCF-7, HeLa and HCT 116 cancer cell line. Cancer Nanotechnol 12(1):33. https://doi.org/10.1186/s12645-021-00106-7

Jia J, Liu X, Wu K, Zhou X, Ge F (2019) Loading zedoary oil into pH-sensitive chitosan grafted mesoporous silica nanoparticles via gate-penetration by supercritical CO2 (GPS). J CO2 Util 33:12–20. https://doi.org/10.1016/j.jcou.2019.05.010

Joseph Emil, Singhvi Gautam (2019) Chapter 4—Multifunctional nanocrystals for cancer therapy: a potential nanocarrier. In: Grumezescu AM (ed) Nanomaterials for drug delivery and therapy. William Andrew Publishing, Norwich, pp 91–116

Klein G, Vellenga E, Fraaije MW, Kamps WA, de Bont ES (2004) The possible role of matrix metalloproteinase (MMP)-2 and MMP-9 in cancer, e.g. acute leukemia. Crit Rev Oncol Hematol 50(2):87–100. https://doi.org/10.1016/j.critrevonc.2003.09.001

Kopp F, Mendell JT (2018) Functional classification and experimental dissection of long noncoding RNAs. Cell 172(3):393–407. https://doi.org/10.1016/j.cell.2018.01.011

Kossakowska AE, Edwards DR, Prusinkiewicz C, Zhang MC, Guo D, Urbanski SJ, Grogan T, Marquez LA, Janowska-Wieczorek A (1999) Interleukin-6 regulation of matrix metalloproteinase (MMP-2 and MMP-9) and tissue inhibitor of metalloproteinase (TIMP-1) expression in malignant non-Hodgkin's lymphomas. Blood 94(6):2080–2089. https://doi.org/10.1182/blood.V94.6.2080

Kulshrestha A, Katara GK, Ibrahim SA, Patil R, Patil SA, Beaman KD (2017) Microtubule inhibitor, SP-6-27 inhibits angiogenesis and induces apoptosis in ovarian cancer cells. Oncotarget 8(40):67017–67028. https://doi.org/10.18632/oncotarget.17549

Lammari N, Louaer O, Meniai AH, Elaissari A (2020) Encapsulation of essential oils via nanoprecipitation process: overview, progress, challenges and prospects. Pharmaceutics. https://doi.org/10.3390/pharmaceutics12050431

Lee DJ, Zeidner JF (2019) Cyclin-dependent kinase (CDK) 9 and 4/6 inhibitors in acute myeloid leukemia (AML): a promising therapeutic approach. Expert Opin Investig Drugs 28(11):989–1001. https://doi.org/10.1080/13543784.2019.1678583

Li J, Liu F, Shao Q, Min Y, Costa M, Yeow EK (2014) Enzyme-responsive cell-penetrating peptide conjugated mesoporous silica quantum dot nanocarriers for controlled release of nucleus-targeted drug molecules and real-time intracellular fluorescence imaging of tumor cells. Adv Healthc Mater 3(8):1230–9. https://doi.org/10.1002/adhm.201300613

Li H, Yu B, Li J, Su L, Yan M, Zhu Z, Liu B (2014a) Overexpression of lncRNA H19 enhances carcinogenesis and metastasis of gastric cancer. Oncotarget 5(8):2318–2329. https://doi.org/10.18632/oncotarget.1913

Li J, Wu S, Wu C, Qiu L, Zhu G, Cui C (2016) Versatile surface engineering of porous nanomaterials with bioinspired polyphenol coatings for targeted and controlled drug delivery. Nanoscale. https://doi.org/10.1039/c6nr00600k

Li D, Luo Y, Chen X, Zhang L, Wang T, Zhuang Y, Fan Y, Xu J, Chen Y, Wu L (2019) NF-κB and Poly (ADP-ribose) polymerase 1 form a positive feedback loop that regulates DNA repair in acute myeloid leukemia cells. Mol Cancer Res 17(3):761–772. https://doi.org/10.1158/1541-7786.mcr-18-0523

Li Z, Wen W, Chen X, Zhu L, Cheng G, Liao Z, Huang H, Ming L (2020) Release characteristics of an essential oil component encapsulated with cyclodextrin shell matrices. Curr Drug Deliv. https://doi.org/10.2174/1567201817666200731164902

Lin L-I, Lin D-T, Chang C-J, Lee C-Y, Tang J-L, Tien H-F (2002) Marrow matrix metalloproteinases (MMPs) and tissue inhibitors of MMP in acute leukaemia: potential role of MMP-9 as a surrogate marker to monitor leukaemic status in patients with acute myelogenous leukaemia. Br J Haematol 117(4):835–841. https://doi.org/10.1046/j.1365-2141.2002.03510.x

Ling-Li W, Bing Z, Ming-Hua Z, Yu-Zhong X, Wang J-J, Jing-Yi J (2020) Matrix metalloproteinases (MMPs) in targeted drug delivery: synthesis of a potent and highly selective inhibitor against matrix metalloproteinase- 7. Curr Top Med Chem 20(27):2459–2471. https://doi.org/10.2174/1568026620666200722104928

Liu Z, Chen Q, Hann SS (2019) The functions and oncogenic roles of CCAT1 in human cancer. Biomed Pharmacother 115:108943. https://doi.org/10.1016/j.biopha.2019.108943

Livak KJ, Schmittgen TD (2001) Analysis of relative gene expression data using real-time quantitative PCR and the 2(-Delta Delta C(T)) Method. Methods 25(4):402–408. https://doi.org/10.1006/meth.2001.1262

Losso JN, Khachatryan A, Masahiro Ogawa J, Godber S, Shih F (2005) Random centroid optimization of phosphatidylglycerol stabilized lutein-enriched oil-in-water emulsions at acidic pH. Food Chem 92(4):737–744. https://doi.org/10.1016/j.foodchem.2004.12.029

Lu Y, Chen J, Xiao M, Li W, Miller DD (2012) An overview of tubulin inhibitors that interact with the colchicine binding site. Pharm Res 29(11):2943–2971. https://doi.org/10.1007/s11095-012-0828-z

Lu Y, Li Y, Chai X, Kang Q, Zhao P, Xiong J, Wang J (2017) Long noncoding RNA HULC promotes cell proliferation by regulating PI3K/AKT signaling pathway in chronic myeloid leukemia. Gene 607:41–46. https://doi.org/10.1016/j.gene.2017.01.004

Matshetshe KI, Parani S, Manki SM, Oluwafemi OS (2018) Preparation, characterization and in vitro release study of β-cyclodextrin/chitosan nanoparticles loaded Cinnamomum zeylanicum essential oil. Int J Biol Macromol 118(Pt A):676–682. https://doi.org/10.1016/j.ijbiomac.2018.06.125

McIlwain DR, Berger T, Mak TW (2013) Caspase functions in cell death and disease. Cold Spring Harb Perspect Biol 5(4):a008656. https://doi.org/10.1101/cshperspect.a008656

McMahon HT, Boucrot E (2011) Molecular mechanism and physiological functions of clathrin-mediated endocytosis. Nat Rev Mol Cell Biol 12(8):517–533. https://doi.org/10.1038/nrm3151

Melendez-Rodriguez B, Figueroa-Lopez KJ, Bernardos A, Martínez-Máñez R, Cabedo L, Torres-Giner S, Lagaron JM (2019) Electrospun antimicrobial films of poly(3-hydroxybutyrate-co-3-hydroxyvalerate) containing eugenol essential oil encapsulated in mesoporous silica nanoparticles. Nanomaterials. https://doi.org/10.3390/nano9020227

Morales J, Li L, Fattah FJ, Dong Y, Bey EA, Patel M, Gao J, Boothman DA (2014) Review of poly (ADP-ribose) polymerase (PARP) mechanisms of action and rationale for targeting in cancer and other diseases. Crit Rev Eukaryot Gene Expr 24(1):15–28. https://doi.org/10.1615/critreveukaryotgeneexpr.2013006875

Niu W, Wang J, Wang Q, Shen J (2020) Celastrol loaded nanoparticles with ROS-response and ROS-inducer for the treatment of ovarian cancer. Front Chem 8:901

Ossovskaya V, Koo IC, Kaldjian EP, Alvares C, Sherman BM (2010) Upregulation of poly (ADP-Ribose) polymerase-1 (PARP1) in triple-negative breast cancer and other primary human tumor types. Genes Cancer 1(8):812–821. https://doi.org/10.1177/1947601910383418

Panzitt K, Tschernatsch MMO, Guelly C, Moustafa T, Stradner M, Strohmaier HM, Buck CR, Denk H, Schroeder R, Trauner M, Zatloukal K (2007) Characterization of HULC, a novel gene with striking up-regulation in hepatocellular carcinoma, as noncoding RNA. Gastroenterology 132(1):330–342. https://doi.org/10.1053/j.gastro.2006.08.026

Perillo B, Di Donato M, Pezone A, Di Zazzo E, Giovannelli P, Galasso G, Castoria G, Migliaccio A (2020) ROS in cancer therapy: the bright side of the moon. Exp Mol Med 52(2):192–203. https://doi.org/10.1038/s12276-020-0384-2

Pham H, Ramos K, Sua A, Acuna J, Slowinska K, Nguyen T, Bui A, Weber MDR, Tian F (2020) Tuning crystal structures of iron-based metal-organic frameworks for drug delivery applications. ACS Omega 5(7):3418–3427. https://doi.org/10.1021/acsomega.9b03696

Popovici RA, Vaduva D, Pinzaru I, Dehelean CA, Farcas CG, Coricovac D, Danciu C, Popescu I, Alexa E, Lazureanu V, Stanca HT (2019) A comparative study on the biological activity of essential oil and total hydro-alcoholic extract of Satureja hortensis L. Exp Ther Med 18(2):932–942. https://doi.org/10.3892/etm.2019.7635

Raveh E, Matouk IJ, Gilon M, Hochberg A (2015) The H19 Long non-coding RNA in cancer initiation, progression and metastasis – a proposed unifying theory. Mol Cancer 14(1):184. https://doi.org/10.1186/s12943-015-0458-2

Richter A, Schoenwaelder N, Sender S, Junghanss C, Maletzki C (2021) Cyclin-dependent kinase inhibitors in hematological malignancies-current understanding, (Pre-)clinical application and promising approaches. Cancers (Basel). https://doi.org/10.3390/cancers13102497

Robinson AJ, Hopkins GL, Rastogi N, Hodges M, Doyle M, Davies S, Hole PS, Omidvar N, Darley RL, Tonks A (2020) Reactive oxygen species drive proliferation in acute myeloid leukemia via the glycolytic regulator PFKFB3. Cancer Res 80(5):937–949. https://doi.org/10.1158/0008-5472.can-19-1920

Rothstein SN, Federspiel WJ, Little SR (2009) A unified mathematical model for the prediction of controlled release from surface and bulk eroding polymer matrices. Biomaterials 30(8):1657–1664. https://doi.org/10.1016/j.biomaterials.2008.12.002

Sahay G, Alakhova DY, Kabanov AV (2010) Endocytosis of nanomedicines. J Control Release 145(3):182–195. https://doi.org/10.1016/j.jconrel.2010.01.036

Sattary M, Amini J, Hallaj R (2020) Antifungal activity of the lemongrass and clove oil encapsulated in mesoporous silica nanoparticles against wheat's take-all disease. Pesticide Biochem Physiol 170:104696. https://doi.org/10.1016/j.pestbp.2020.104696

Scherr AL, Gdynia G, Salou M, Radhakrishnan P, Duglova K, Heller A, Keim S, Kautz N, Jassowicz A, Elssner C, He YW, Jaeger D, Heikenwalder M, Schneider M, Weber A, Roth W, Schulze-Bergkamen H, Koehler BC (2016) Bcl-xL is an oncogenic driver in colorectal cancer. Cell Death Amp Dis 7:e2342. https://doi.org/10.1038/cddis.2016.233

Shahein SA, Aboul-Enein AM, Higazy IM, Abou-Elella F, Lojkowski W, Ahmed ER, Mousa SA, AbouAitah K (2019) Targeted anticancer potential against glioma cells of thymoquinone delivered by mesoporous silica core-shell nanoformulations with pH-dependent release. Int J Nanomed 14:5503–5526. https://doi.org/10.2147/IJN.S206899

Shaker OG, Senousy MA, Elbaz EM (2017) Association of rs6983267 at 8q24, HULC rs7763881 polymorphisms and serum lncRNAs CCAT2 and HULC with colorectal cancer in Egyptian patients. Sci Rep 7(1):16246. https://doi.org/10.1038/s41598-017-16500-4

Shao Y, Luo W, Guo Q, Li X, Zhang Q, Li J (2019) In vitro and in vivo effect of hyaluronic acid modified, doxorubicin and gallic acid co-delivered lipid-polymeric hybrid nano-system for leukemia therapy. Drug Des Dev Ther 13:2043–2055. https://doi.org/10.2147/DDDT.S202818

Shetta A, Kegere J, Mamdouh W (2019) Comparative study of encapsulated peppermint and green tea essential oils in chitosan nanoparticles: encapsulation, thermal stability, in-vitro release, antioxidant and antibacterial activities. Int J Biol Macromol 126:731–742. https://doi.org/10.1016/j.ijbiomac.2018.12.161

Siegel RL, Miller KD, Jemal A (2016) Cancer statistics, 2016. CA Cancer J Clin 66(1):7–30. https://doi.org/10.3322/caac.21332

Sillar JR, Germon ZP, Deluliis GN, Dun MD (2019) The role of reactive oxygen species in acute myeloid leukaemia. Int J Mol Sci 20(23):6003. https://doi.org/10.3390/ijms20236003

Siveen KS, Uddin S, Mohammad RM (2017) Targeting acute myeloid leukemia stem cell signaling by natural products. Mol Cancer 16(1):13. https://doi.org/10.1186/s12943-016-0571-x

Slowing II, Vivero-Escoto JL, Chia-Wen Wu, Lin VSY (2008) Mesoporous silica nanoparticles as controlled release drug delivery and gene transfection carriers. Adv Drug Deliv Rev 60(11):1278–1288. https://doi.org/10.1016/j.addr.2008.03.012

Suminoe A, Matsuzaki A, Hattori H, Koga Y, Ishii E, Hara T (2007) Expression of matrix metalloproteinase (MMP) and tissue inhibitor of MMP (TIMP) genes in blasts of infant acute lymphoblastic leukemia with organ involvement. Leuk Res 31(10):1437–1440. https://doi.org/10.1016/j.leukres.2007.01.015

Tang Q, Hann SS (2018) HOTAIR: an oncogenic long non-coding RNA in human cancer. Cell Physiol Biochem 47(3):893–913. https://doi.org/10.1159/000490131

Tang F, Li L, Chen D (2012) Mesoporous silica nanoparticles: synthesis, biocompatibility and drug delivery. Adv Mater 24(12):1504–1534. https://doi.org/10.1002/adma.201104763

Tsai WC, Hsu SD, Hsu CS, Lai TC, Chen SJ, Shen R, Huang Y, Chen HC, Lee CH, Tsai TF, Hsu MT, Wu JC, Huang HD, Shiao MS, Hsiao M, Tsou AP (2012) MicroRNA-122 plays a critical role in liver homeostasis and hepatocarcinogenesis. J Clin Invest 122(8):2884–2897. https://doi.org/10.1172/jci63455

Vaux DL, Cory S, Adams JM (1988) Bcl-2 gene promotes haemopoietic cell survival and cooperates with c-myc to immortalize pre-B cells. Nature 335(6189):440–442. https://doi.org/10.1038/335440a0

Vieira R, Severino P, Nalone LA, Souto SB, Silva AM, Lucarini M, Durazzo A, Santini A, Souto EB (2020) Sucupira oil-loaded nanostructured lipid carriers (NLC): lipid screening, factorial design, release profile, and cytotoxicity. Molecules. https://doi.org/10.3390/molecules25030685

Vu HT, Hoang TX, Kim JY (2018) All-trans retinoic acid enhances matrix metalloproteinase 2 expression and secretion in human myeloid leukemia THP-1 cells. Biomed Res Int 2018:5971080. https://doi.org/10.1155/2018/5971080

Wang J, Liu X, Huacheng Wu, Ni P, Zhidong Gu, Qiao Y, Chen N, Sun F, Fan Q (2010) CREB up-regulates long non-coding RNA, HULC expression through interaction with microRNA-372 in liver cancer. Nucleic Acids Res 38(16):5366–5383. https://doi.org/10.1093/nar/gkq285

Watkins R, Wu L, Zhang C, Davis RM, Xu B (2015) Natural product-based nanomedicine: recent advances and issues. Int J Nanomedicine 10:6055–6074. https://doi.org/10.2147/ijn.s92162

Wei CL, Wu Q, Vega VB, Chiu KP, Ng P, Zhang T, Shahab A, Yong HC, Fu Y, Weng Z, Liu J, Zhao XD, Chew JL, Lee YL, Kuznetsov VA, Sung WK, Miller LD, Lim B, Liu ET, Yu Q, Ng HH, Ruan Y (2006) A global map of p53 transcription-factor binding sites in the human genome. Cell 124(1):207–219. https://doi.org/10.1016/j.cell.2005.10.043

Woo CJ, Kingston RE (2007) HOTAIR lifts noncoding RNAs to new levels. Cell 129(7):1257–1259. https://doi.org/10.1016/j.cell.2007.06.014

Xie W, Zhang C (2016) Propylsulfonic and arenesulfonic functionalized SBA-15 silica as an efficient and reusable catalyst for the acidolysis of soybean oil with medium-chain fatty acids. Food Chem 211:74–82. https://doi.org/10.1016/j.foodchem.2016.05.025

Yasinska IM, Ceccone G, Ojea-Jimenez I, Ponti J, Hussain R, Siligardi G, Berger SM, Fasler-Kan E, Bardelli M, Varani L, Fiedler W, Wellbrock J, Raap U, Gibbs BF, Calzolai L, Sumbayev VV (2018) Highly specific targeting of human acute myeloid leukaemia cells using pharmacologically active nanoconjugates. Nanoscale 10(13):5827–5833. https://doi.org/10.1039/C7NR09436A

Zhang TJ, Zhou JD, Zhang W, Lin J, Ma JC, Wen XM, Yuan Q, Li XX, Xu ZJ, Qian J (2018) H19 overexpression promotes leukemogenesis and predicts unfavorable prognosis in acute myeloid leukemia. Clin Epigenetics 10:47. https://doi.org/10.1186/s13148-018-0486-z

Zhao TT, Liu X (2019) LncRNA-H19 inhibits apoptosis of acute myeloid leukemia cells via targeting miR-29a-3p. Eur Rev Med Pharmacol Sci 23(3 Suppl):224–231. https://doi.org/10.26355/eurrev_201908_18651

Zhou S, Wu D, Yin X, Jin X, Zhang X, Zheng S, Wang C, Liu Y (2017) Intracellular pH-responsive and rituximab-conjugated mesoporous silica nanoparticles for targeted drug delivery to lymphoma B cells. J Exp Clin Cancer Res 36(1):24. https://doi.org/10.1186/s13046-017-0492-6

Publisher's Note

Springer Nature remains neutral with regard to jurisdictional claims in published maps and institutional affiliations.